

University of Groningen

Dissecting dynamic interactions between metabolic and cell cycle oscillators: development and application of novel single-cell tools

Chen, Haoqi

DOI:

[10.33612/diss.207591836](https://doi.org/10.33612/diss.207591836)

IMPORTANT NOTE: You are advised to consult the publisher's version (publisher's PDF) if you wish to cite from it. Please check the document version below.

Document Version

Publisher's PDF, also known as Version of record

Publication date:

2022

[Link to publication in University of Groningen/UMCG research database](#)

Citation for published version (APA):

Chen, H. (2022). *Dissecting dynamic interactions between metabolic and cell cycle oscillators: development and application of novel single-cell tools*. [Thesis fully internal (DIV), University of Groningen]. University of Groningen. <https://doi.org/10.33612/diss.207591836>

Copyright

Other than for strictly personal use, it is not permitted to download or to forward/distribute the text or part of it without the consent of the author(s) and/or copyright holder(s), unless the work is under an open content license (like Creative Commons).

The publication may also be distributed here under the terms of Article 25fa of the Dutch Copyright Act, indicated by the "Taverne" license. More information can be found on the University of Groningen website: <https://www.rug.nl/library/open-access/self-archiving-pure/taverne-amendment>.

Take-down policy

If you believe that this document breaches copyright please contact us providing details, and we will remove access to the work immediately and investigate your claim.

Downloaded from the University of Groningen/UMCG research database (Pure): <http://www.rug.nl/research/portal>. For technical reasons the number of authors shown on this cover page is limited to 10 maximum.

Chapter 4

The dynamics and functions of the second-messenger cAMP during the yeast cell cycle

Haoqi Chen, Suzanne Jansen, Enrico Calzati, Andreas Miliias-Argeitis, Matthias Heinemann

1 Molecular Systems Biology, Groningen Biomolecular Sciences and Biotechnology Institute, University of Groningen, Nijenborgh 4, 9747 AG Groningen, The Netherlands

* Lead Contact: Phone: +31 50 363 8146, Twitter: @HeinemannLab, E-mail: m.heinemann@rug.nl

Abstract

Eukaryotic cell cycle progression is known to be coordinated by the cyclin/cyclin-dependent kinase (CDK) machinery. Recently, however, metabolism was found to be an autonomous oscillator that potentially co-regulates the cell cycle. How such co-regulation is accomplished is still unknown. Signaling pathways, given their function in both sensing intracellular metabolites and regulating cell growth, are potential molecular mechanisms underlying such co-regulation. In this study, we investigated the dynamics and function of the second-messenger cAMP during the yeast cell cycle. Using Msn2, a transcriptional activator whose localization is controlled by protein kinase A (PKA)-dependent phosphorylation, and a FRET cAMP sensor, we showed that cAMP levels are constant and high when cells are cultured on glucose. In contrast, cAMP levels oscillate and peak around budding on acetate. By controlling cAMP production with optogenetics, we further showed that cAMP is essential for initiating but not finishing the cell cycle, revealing a specific link between cAMP concentration and early cell cycle regulation. Our results suggest that cAMP/PKA activity is part of a check-point mechanism of cell cycle initiation. We anticipate that this knowledge can serve as a starting point to reveal how metabolism and cell cycle regulation are coupled.

Introduction

Metabolism was found to oscillate in strict synchrony with cell cycle progression, whenever cells divided¹. We have found that the temporal segregation of key biosynthetic processes, i.e., lipid, polysaccharide and protein synthesis proceeding at different rates during the cell cycle, is responsible for the oscillations observed in primary carbon and energy metabolism². The metabolic oscillations were found to have a role in cell cycle control, for example, by interacting with early and late cell cycle elements³.

Thus, a key question now is what drives these metabolic oscillations. We found that the metabolic oscillations are not caused by the cell cycle machinery, as they also occurred when the cell cycle progression was halted by depletion of key regulators of certain cell cycle phases^{1,3}. Alternatively, they could be caused by a transcriptional oscillator^{4,5}. Further, also signaling pathways that pick up intracellular signals and exert regulatory action, could potentially be part of a mechanism that generates the cell-cycle autonomous metabolic/biosynthetic oscillations.

One of these signaling pathways that is increasingly recognized to also sense intracellular signals is the cAMP/PKA pathway. In the budding yeast *Saccharomyces cerevisiae*, the cAMP/PKA pathway receives signals of and responds to changes in environmental glucose concentration⁶, via either a G-protein coupled receptor or cytoplasm acidification and subsequent activation of Ras1,2 proteins^{6,7}. cAMP/PKA subsequently regulates cell growth by tuning downstream gene expression, for example by promoting ribosome biogenesis or suppressing stress-responsive genes⁶. Recently, fructose-1,6-bisphosphate (FBP), a reporter metabolite of glycolytic flux⁸, has also been found to activate Ras via the Cdc25 guanine nucleotide exchange factor (GEF)⁹. Thus, the cAMP/PKA pathway, by connecting an intracellular signal (as opposed to environmental signals) to cell growth, could be part of the metabolic oscillations.

In fact, the dynamics of this signaling pathway and its involvement in carbon storage metabolism during the cell cycle has been studied on the population level. Measurements in synchronized yeast cells grown on glucose-limited conditions, obtained by either continuous chemostat culture or by elutriation, have revealed oscillations in cAMP levels during the cell cycle¹⁰. Yet, whether such oscillations exist in elutriated cultures grown on high glucose condition was less clear. The oscillations observed on glucose-limited conditions were synchronized with the synthesis-liquidation cycle of trehalose and glycogen. Based on this evidence, the “finishing kick-to-START” model of cell cycle control has been proposed¹¹. However, it was later estimated that, except for the nutritionally-harsh growth conditions such as those found in glucose-limited chemostat cultures or

when approaching stationary phase where cells show a very slow growth rate, the amount of trehalose and glycogen stored was too low to affect the progression of cell cycle¹². Supporting this observation, mutants unable to synthesize carbon storage are viable with a normal growth rate on ethanol¹³ (Notably, however, on glucose a Δ TPS1 knockout strain would show aberrant growth, not due to the lack of carbon storage, but due to imbalanced reactions in glycolysis pathway which could be rescued by a Hxk2 mutation¹⁴). Further, the CDK machinery was found to directly regulate the utilization of stored carbon, by phosphorylating Nth1 and likely also Gph1, the main enzymes liquidizing trehalose and glycogen^{12,13}. Therefore, controlling the synthesis-liquidation cycle of trehalose and glycogen is unlikely the main function of PKA pathway during a normal cell cycle. Thus, overall, it is unclear what the role is of the cAMP/PKA during the cell cycle.

Here, we investigated the dynamics and function of the second messenger cAMP during the cell cycle. We conducted our investigation at the single-cell level to avoid confounding factors such as imperfect synchronization, which is inherently present in population-level studies¹⁰. Using the Msn2 transcription factor and a FRET sensor as readout, we found that cAMP concentration oscillates on acetate, while remaining relatively steady on high glucose. Further, by dynamically controlling cAMP synthesis with optogenetics, we observed that cAMP is essential to the early but not the late phase of the cell cycle. The results revealed for the first time the dynamics of cAMP concentration during the cell cycle on single-cell level and different nutrient conditions, and provided preliminary evidence on the function of the cAMP/PKA pathway in cell cycle regulation.

Results

Msn2 as a reporter of cAMP/PKA activity in single cells

Msn2 is a transcription factor whose nuclear localization is induced by stress conditions/low PKA activity¹⁵, and as such, its nuclear localization can be used as a proxy for cAMP/PKA activity. To monitor the output of the cAMP/PKA pathway in single cells, we tagged Msn2 with two different fluorescent proteins. To verify that cAMP concentration could affect Msn2 localization, we perturbed cAMP production by dynamic depletion of the adenylate cyclase *Cyr1*, i.e., the enzyme that produces cAMP. For this, we added a degron tag to *Cyr1* and induced its depletion by addition of auxin^{16–18}. At the same time, we introduced in the same strain a bacterial photo-activatable adenylate cyclase (bPAC)^{19,20}. With this strain, we could first dynamically remove the native adenylate cyclase, upon which no more cAMP is produced. Then, by turning on blue light, we could activate the bPAC to abruptly resynthesize cAMP. By following the localization of Msn2 during these perturbations, we aimed to validate the connection between cAMP levels and Msn2 localization.

Before we could do so, we first had to establish a method to identify and quantify the nuclear accumulation of Msn2. Here, we calculated and tested various indices for quantifying nuclear localization of a fluorescently tagged proteins from microscopy images. The indices were either directly derived from literature^{20,21} or created by modification and/or combination of the former (Table S3). To compare the performance of these indices, we determined visually in a number of cells whether Msn2 was localized in the nucleus or cytoplasm, and created a test dataset. Then, we computed each localization index for each of the cells in the test set. We identified a threshold value for each index, so that we could obtain optimal localization classification with minimal false positive and false negative categorization (Fig. S1A). The different indices were then compared by their false categorization rate to select the best-performing one (Fig. S1B). By this process, we identified the Stewart parameter (S-parameter), which is calculated by dividing the mean intensity of the 10% brightest pixels by the median intensity of all pixels in a cell²⁰, as the best-performing index. We determined the localization threshold for each movie separately using its own training dataset, to correct for minor differences caused by different imaging settings (e.g., use of different fluorescent proteins).

We found that vacuoles could be a confounding factor to the determination of Msn2 nuclear localization. When a large vacuole covers a large proportion of cytosolic volume, cytosolic fluorescently tagged Msn2 can appear more concentrated and form a bright spot that might lead to a misclassification of its localization. To alleviate this problem, we further tagged the histone H2A with a red fluorescent protein (mRFP1) to directly visualize the nucleus¹. We then determined the amount of GFP-tagged Msn2 signal inside

the nucleus and in the cytosol, and used the nuclear to cytosolic ratio as an alternative metric to the S-parameter for determining Msn2 nucleus localization. Both indices were used in parallel, to avoid any bias that one index alone could introduce.

It has been reported that cAMP/PKA-Msn2 is a pathway that senses light-induced stress²². As we used light to determine the nuclear localization of Msn2, we had to check for potential confounding effect of light-toxicity. Therefore, we measured the energy of the GFP excitation light with our imaging settings, which was found to be 0.076 J/cm² (Fig. S2), lower than a condition (0.16 J/cm²) that were previously reported to not cause toxicity²², thus is safe for the cell. Furthermore, since we were imaging at a lower frequency (1 frame/5 minutes) than the light-toxicity free condition (1 frame/30 s)²², we will not accumulate light-toxicity over time, so we concluded that our imaging setting was unlikely to induce light toxicity. Further, to experimentally confirm that light toxicity was not induced over the course of the full experiments (12-20 hours), the fraction of cells with high Msn2 nuclear localization over the course of the movie was determined for each experiment, and showed no overall increase, indicating no accumulation of light-induced stress (Fig. S3). Finally, we also constructed a strain with mVenus-tagged Msn2 and performed the same experiments to rule out potential light-toxicity effects, since mVenus is excited by green light that is less toxic than blue light²³.

Equipped with these tools and methods, we then aimed to verify the link between cAMP concentration and Msn2 localization. As cAMP is produced via the adenylate cyclase Cyr1, we perturbed cAMP concentration by depleting Cyr1 with an auxin-degron system. First, cells grown on glucose were left unperturbed for around four hours, and then auxin was added to the medium, leading to depletion of proteins that carried the degradation tag. A control strain expressing a degron-tagged GFP that was loaded in the same chip, indicated the precise time of auxin arrival and protein depletion (Fig. 1A). During the phase prior to the perturbation, we found that Msn2 was mainly localized in the cytoplasm, with stochastic translocation events into the nucleus, as shown by the S-parameter (Fig. 1B, C, gray shading). By adding auxin to the medium to deplete Cyr1, Msn2 rapidly shuttled into the nucleus (Fig. 1B, C, no shading) and stayed there. In a second experiment, we performed the same initial treatment, but after 150 minutes of Cyr1 depletion (time of depletion indicated by Fig. 1D) we activated the light-inducible adenylate cyclase bPAC with blue light, and thereby restored cAMP production. Here, we found that Msn2 immediately returned to the cytoplasm (Fig. 1E, F). This confirmed that Msn2 localization is a direct consequence of altered cAMP levels. As such, Msn2 localization is a reporter of cAMP/PKA activity.

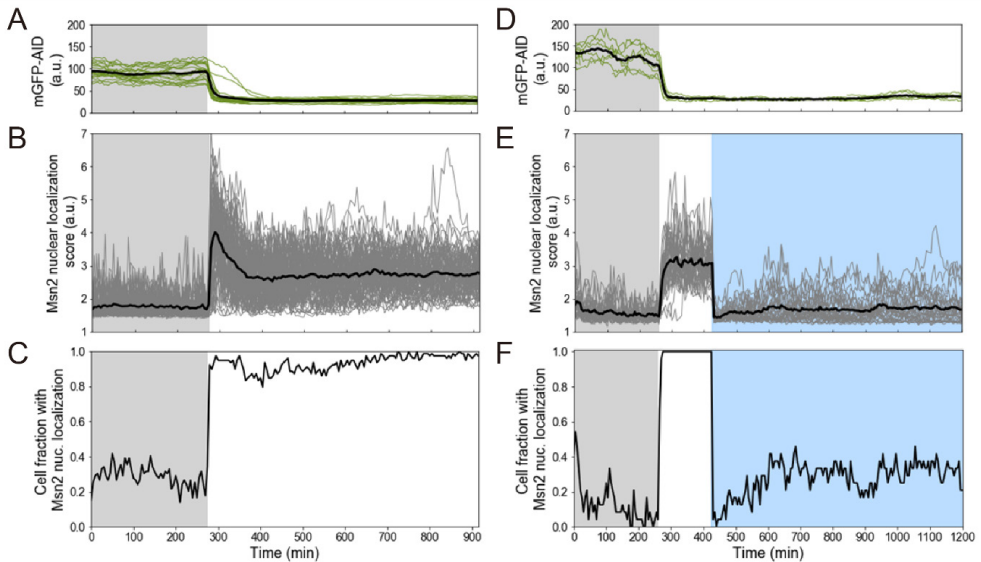


Fig. 1: Msn2 is a reporter of intracellular cAMP level. (A) A strain expressing mGFP-AID (auxin-induced degron) was used to determine the time of auxin induced protein depletion. Black line shows the average mGFP fluorescence intensity (a.u.) of 21 cells (green lines). (B) Nuclear localization score (S-parameter) of Msn2 after inhibition of the cAMP/PKA pathway by Cyr1-AID depletion. Thick black line shows average Msn2 localization score of 79 cells with single cell trajectories (thin grey lines). (C) Cell fraction (79 cells, from 1B) with nuclear localization of Msn2 (determined on the basis of the S-parameter) approaches 1 upon Cyr1-AID depletion. (D) As in (A) (11 mGFP-AID cells). (E) Nuclear localization of Msn2 after inhibition of the cAMP/PKA pathway by Cyr1-AID and subsequent Msn2 delocalization caused by blue light activation of bPAC. Thick black line shows average Msn2 localization score of 40 cells with single cell trajectories (thin grey lines). (F) Cell fraction (24 cells, from 1E) with nuclear localization of Msn2 stabilizes around 0.30 upon bPAC activation by blue light.

Msn2 localization during the cell cycle on different conditions

To investigate cAMP concentration and thus PKA activity dynamics during the cell cycle, we observed Msn2 localization in single yeast cells cultured with either high glucose, where cells use a fermentative metabolism, or with acetate, where cells use a respiratory metabolism). For each condition, we performed the experiment with an Msn2-tdGFP strain and an Msn2-mVenus strain. For each experiment, the specific S-parameter threshold for characterizing the Msn2 nuclear localization was determined as described above. Using two adjacent budding events, we segmented each cell cycle and aligned them from on budding even to the next, such that each cell cycle progressed on a normalized time scale ranging from 0 to 1.

With both tagging methods, we found that Msn2 is mostly localized in the cytoplasm (Fig. 2A) on high glucose, indicating a high overall cAMP concentration. Furthermore, Msn2 localization was rather constant throughout the cell cycle, indicating that the cAMP/PKA

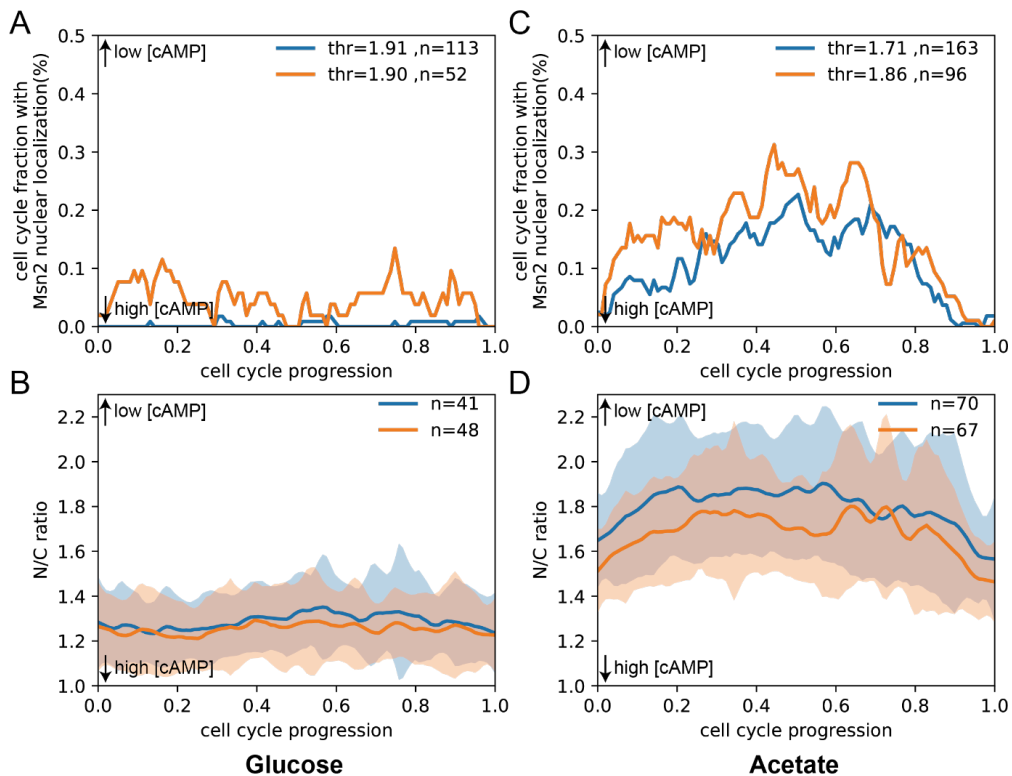


Fig. 2: Msn2 localization during the cell cycle on glucose and acetate. (A) On glucose, the fraction of cell cycles with Msn2 localized to the nucleus (as determined using the S-parameter, namely ratio of the median intensity of all pixels to the mean intensity of the 10% brightest pixels in a cell) is relatively low and steady throughout the cell cycle. Lower Msn2 nucleus localization fraction indicates a higher cellular cAMP concentration. Blue and orange lines are results obtained by tagging Msn2 with either tdGFP or mVenus, respectively. For the experiment that used tdGFP as the reporter (blue curve), a large number of Msn2 localization events was falsely determined due to complication of vacuoles, and these events were manually tracked, corrected as not-localized and the data from the corresponding cell cycles was included in analysis. (B) On glucose, the nucleus-to-cytoplasmic ratio (calculated after subtraction of autofluorescence) of Msn2 fluorescence (tagged by tdGFP) is also relatively low and steady throughout the cell cycle. A lower ratio indicates a higher cellular cAMP concentration. Shading indicates the range of standard deviation over the number of cell cycles analyzed. Blue and orange curves/shading represent results from two replicated experiments. (C) On acetate, the fraction of cell cycles with Msn2 nucleus localization oscillates and peaked at late cell cycle (0.5 ~ 0.6, while for an averaged cell cycle mitotic exits would occur around 0.64). Color scheme is the same as in (A). (D) On acetate, the nucleus-to-cytoplasmic ratio of Msn2 is higher than that on glucose, and oscillates throughout the cell cycle in a similar pattern as when determined by the S-parameter. Color scheme and shading are the same as in (B).

pathway is constitutively active. We further validated this result using the nucleus-to-cytoplasmic ratio of *Msn2-tdGFP* fluorescence (N/C ratio) in the strain where the histone (H2A) was tagged with mRFP1. Here, we obtained results consistent with the one obtained with the S-parameter (Fig. 2B), namely, that the N/C ratio remained constantly at a low level, indicating a high and steady cAMP concentration during the cell cycle.

On acetate, however, Msn2 localization was found to oscillate during the cell cycle with both tagging methods, with its trough occurring at budding and the peak occurring before mitotic exit (Fig. 2C). Similarly, the N/C ratio was found to oscillate during the cell cycle, with the trough at the budding and the peak before mitotic exit (Fig. 2D). These results indicate a rising cAMP concentration, and thus PKA activity, in the early cell cycle, which peaks at budding and then gradually decreases as cells progress towards the end of the cell cycle. Further, the cell fraction with Msn2 localized in the nucleus (Fig. 2C), as well as the N/C ratio (Fig. 2D), are overall higher in acetate when compared to glucose, suggesting an overall lower cAMP concentration/PKA activity.

Using a FRET sensor to monitor cAMP level during the cell cycle: confounding effect of partially mature species

Although Msn2 localization is known to be controlled by PKA phosphorylation, it could also be affected by other factors, such as by the change in dephosphorylation activity of phosphatase PPI²⁴. Therefore, to further validate the cell cycle dynamics of cAMP/PKA pathway, we also used a recently reported yeast-optimized FRET sensor for cAMP (yEPAC)²⁵ with the aim to directly measure cellular cAMP concentrations. To do so, we introduced plasmids containing either the sensor or a non-responsive mutant (yEPAC-R279L) into the auxotrophic strain YSBN10²⁶, obtaining two strains, which are hence referred as the sensor strain or the mutant strain. The R279L mutation is located in the cAMP-binding domain of Epac1 and locks Epac1 in an autoinhibited conformation²⁷. Both the sensor and the no-responsive mutant are expressed from a plasmid, driven by a *Pmai* promoter. To validate the response of the sensor with our experimental setting (e.g., medium and microscope setting), we performed a nutrient shift experiment from pyruvate to glucose. The sensor strain and the mutant strain were cultured using pyruvate as the carbon source under the microscope, and the steady-state FRET ratio (defined as fluorescence of the donor (mTurquoise2 Δ) divided by that of the receptor (tdTomato))²⁵ was obtained as done previously. Subsequently, glucose was added to the cells, and a rapid and large increase in FRET ratio was observed in the sensor strain while only a small increase was observed for the mutant strain (Fig. 3A), with the amplitude and the time scales of the responses being similar to previously reported results²⁵. The small increase in the mutant strain can be explained via a change in osmotic pressure²⁵. With this dynamic experiment, we confirmed that the FRET sensor is functional in our strains and experimental conditions.

Before we could use the sensor to monitor the cell-cycle related dynamics of cAMP, we first assessed potential confounding factors. First, since we were using a protein-based sensor, we considered the protein expression dynamics during the cell cycle. Together with cell growth (dilution rate), protein expression determines the dynamics of protein abundance²⁸. Previously, it has been reported that protein expression changes during the

cell cycle. Specifically, for a promoter that is not regulated, such as the synthetic promoter *tetO7*, protein synthesis shows two waves, with the first peak around START and the second peak in the middle of S/G₂/M phase². However, for a promoter that is subjected to regulation, the protein synthesis pattern can be more complex. For example, expression of a fluorescent protein driven by the endogenous promoter TEF1 revealed only the first peak in G₁, but did not show the second peak (unpublished data, Molecular System Biology group). In the current setting, the cell-cycle-dependent synthesis dynamics of the sensor/mutant is unknown, since we did not characterize the Pma1 promoter or the plasmid copy number during the cell cycle. Notably, protein expression (or abundance) dynamics only becomes a confounding factor when intertwined with a second factor, as explained below.

A second factor that we considered was the fluorophore maturation time²⁹. Protein expression dynamics is not a confounding factor, if both the donor and sensor proteins matured at the same rate, because the same number of visible/invisible donor and sensor would always be present regardless of their absolute abundance. When the donor and sensor mature at different rate, the ratio between visible donor and sensor would deviate from 1. Depending on the protein expression and cell growth dynamics, the ratio could change between different time points of the cell cycle, complicating the interpretation of FRET ratio and cAMP dynamics. The two fluorophores used in the yEPAC sensor or the yEPAC-R279L mutant are mTurquoise2Δ and tdTomato, which have an equivalent maturation half-time of 65 minutes (mTurquoise2) and 95 minutes (tdTomato) when measured *in vivo* in *S. cerevisiae* at 30 degrees and fitted with a two-step maturation model (unpublished data, Molecular System Biology group). Therefore, it is necessary to address this complication before using the yEPAC sensor for studying cAMP dynamics in the cell cycle.

To enable quantification and correction for the confounding effects described above, we considered the different species of the yEPAC sensor or the R279L mutant inside the cells of each strain (Fig. 3B): fully mature (both fluorophores mature), partially mature (one fluorophore mature) and immature (both fluorophores immature). Note that the partially mature species can be either a species with mature mTurquoise2Δ (as shown in Fig. 3B) or mature tdTomato (expected to be at a lower proportion because tdTomato has longer maturation half-time than mTurquoise2, and therefore not shown). However, partially mature species with mature tdTomato will not contribute to the overall signal if disregard cross-excitation of tdTomato by the CFP excitation light³⁰ (Fig. S4A). Further, in the sensor strain, each species can either be bound or unbound to cAMP, but the binding only changes the fluorescence of the fully matured species, since no resonance energy transfer can happen between immature fluorophores (Fig. 3B, top). For the mutant strain, none of the species binds cAMP^{25,27}. All species (Fig. 3B), except for the immature ones, are fluorescent and thus will contribute to the overall signal (of either the sensor or the mutant strain).

Together, the maturation time and protein expression dynamics determine the proportions of the different sensor species inside the cell. To see this, let us consider the following four time points (Fig. 3C): at T_1 , only fully mature species exist in both strains (sensor and mutant strains), and half of the sensor molecules are assumed to be bound by cAMP. From T_1 to T_2 , cAMP concentration remains the same, while more proteins are expressed. Due to the relatively slow and different maturation time of the sensor fluorophores, partially mature and immature species exist in the cells. Here, since the intracellular concentration of cAMP is in the micromolar range³¹, it is much higher than the concentration of expressed FRET protein molecules, so the ratio of bound sensor molecules remains the same (assumed to be 50% in all three species). However, due to the presence of the partially mature species, the FRET ratio (donor/sensor), has changed at this time point for both the sensor and the mutant strains. Therefore, we cannot directly use the FRET ratio of the sensor strain to investigate cAMP concentration during the cell cycle.

Further, from T_2 to T_3 , we assumed that all partially mature and immature species have turned into fully-matured species, and cAMP remains the same. Here, despite the higher yEPAC sensor or R279L mutant concentration, the FRET ratio of the sensor and mutant strains remain the same as in T_1 . From T_3 to T_4 , cAMP concentration increases, while the amount and composition of yEPAC sensor or R279L mutant remain the same. Here, more FRET sensor will be bound to cAMP, and the overall FRET ratio will be higher than that of T_3 or T_1 in the sensor strain but not in the mutant strain, correctly reflecting the change in cAMP.

In summary, since the partially mature species do not respond to cAMP dynamics, its presence (highlighted by the rectangle in Fig. 3C, T_2) can distort the FRET ratio and cause it to fail to reflect cAMP concentration, due to the disproportional contribution to the fluorescence value of the CFP channel. Furthermore, due to the dynamic protein expression rate, the amount of partially mature species during the cell cycle can also be dynamic, which further confounds interpretation of the result.

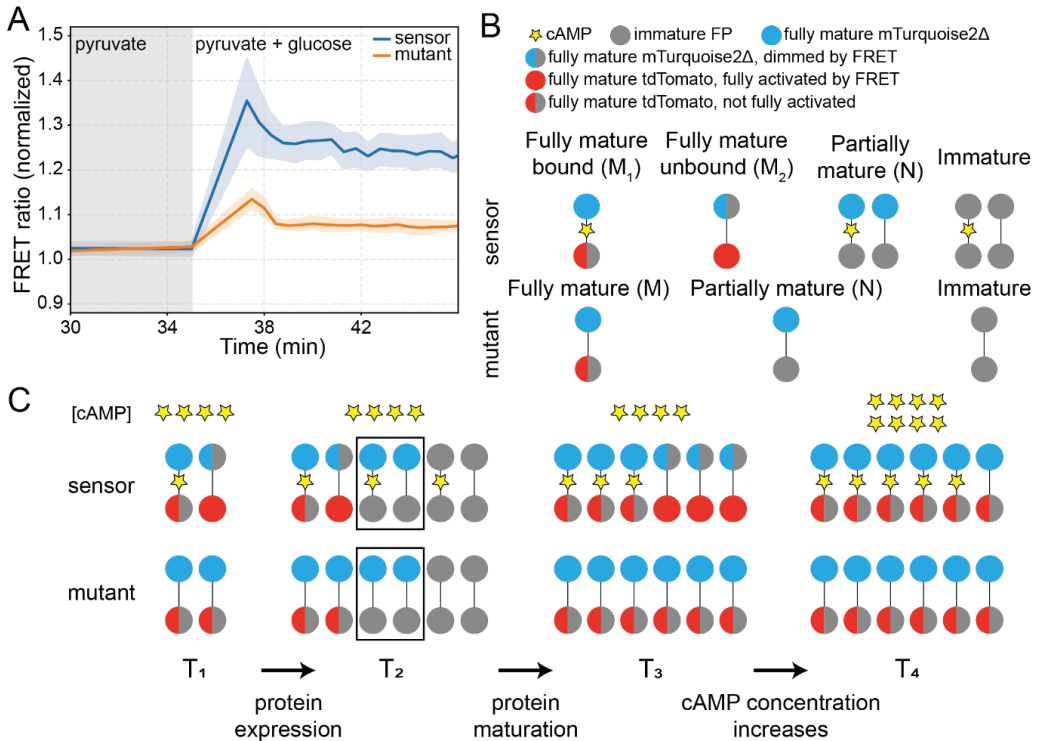


Fig. 3: Establishing a FRET sensor for monitoring cell cycle dynamics of cAMP concentration (A) FRET ratio response to glucose adding, for cells grown in ConA coated wells with minimal medium containing pyruvate. Number of cells analyzed: sensor, $n=17$, mutant, $n=10$. Error bar represent the 95% confidence interval obtained by bootstrapping. Glucose was added at 35.0 minutes, the pipetting of which took around 2.5 minutes, after which the next frame of image was taken. The imaging frequency was set to be 30s/frame after adding glucose. Autofluorescence was estimated from WT cells loaded in the same well and subtracted before calculating FRET ratio. (B) Various species of FRET sensor molecules exist in the cells of both sensor and mutant strains. Yellow star represents cAMP; cyan circle represents mTurquoise2 Δ without FRET while half-cyan circle stands for mTurquoise2 Δ with FRET (and therefore less bright); red circle represents tdTomato with FRET while half-red circle represents tdTomato without FRET (and therefore less bright); grey circle represents immature fluorescent proteins. $M_1/M_2/M/N$ are the numbers of molecules of each indicated species. (C) Four presumed timepoints with different cAMP concentration, protein expression level or protein maturation in the sensor and mutant strains. In T_1 , protein expression level is low, only fully matured species exists for both strains; in T_2 , more proteins are expressed, and there is the same amount of partially mature species in both strains, highlighted by rectangles; in T_3 , the partially mature and immature species have turned into fully matured species; in T_4 , the same species are present as in T_3 . cAMP concentration is assumed the same in the first three timepoints but higher in the fourth timepoints, and in T_1 - T_3 half of each species are assumed to be bound in the sensor strain, while in the fourth timepoints a higher proportion of sensor molecules are bound due to the higher cAMP concentration.

Corrected FRET ratio for removing confounding effect of partially mature species

Since the partially mature species is causing the problem, we could pursue two alternative solutions by removing fluorescence of this species (which is only in the CFP channel). In the first approach, we could build a single-cell model that takes all factors such as protein expression dynamics, protein maturation, cell growth and division into account. This kind of model would allow us to estimate the number of partially mature FRET molecules at each time point inside each single cell. Besides, we would also need to take into account the excitation spectrum, quantum yield, FRET efficiency etc., to estimate the (relative) fluorescence from the partially mature species and removing it. However, at the current stage, we have not characterized the expression dynamics of the sensor, so this approach is not yet feasible.

A second and simpler approach (to remove the partially mature species) is to make use of the mutant strain by subtracting its CFP fluorescence from that of the sensor strain. There are two reasons for doing this: First, since the sensor and mutant strain use the same plasmid and promoter for gene expression and same fluorophores, we can assume that at each cell cycle stages, the composition of species in the two strains (i.e., the numbers of fully-matured, partially mature and immature species) would be the same (assumption 1, see also supplementary text 1) (Fig. 3C). Notably, however, this assumption only holds on the populational level, since single-cell protein expression is stochastic; Second, the fluorescence of the partially mature species is only in the CFP channel (since we did not consider partially mature species with only mature tdTomato, Fig. 3B); Therefore, to eliminate the effect of the partially mature species, we can first calculate the mean CFP fluorescence (by averaging all single cell measurements) of the sensor and mutant strains (CFP_{sensor} , CFP_{mutant}), and then subtract the CFP fluorescence of the mutant strain from that of the sensor strain, before dividing it by the RFP fluorescence of the sensor strain as commonly did in calculating FRET ratio (equation 1, middle term).

We termed this ratio as the “corrected FRET ratio” (equation 1, left and middle terms), which can be calculated from experimental measurements. To understand its relation with the cAMP concentration, we further break the ratio into the concentration (or number of molecules) and fluorescence intensity of each species. Here, to simplify the calculation, we assume that tdTomato is not cross-excited by the CFP excitation light in our experimental setting (and thus do not contribute to the numerator, assumption 2). This leads to the right term of equation 1 (for detailed derivation, refer to supplementary text 1), where CFP_{s1} , CFP_{s2} , CFP_m are mTurquoise2 fluorescence of a single fully mature and cAMP-bound γ EPAC sensor molecule, a single fully mature and unbound γ EPAC sensor molecule, and a single fully mature R279L mutant molecule, respectively. RFP_{s1} , RFP_{s2} are tdTomato fluorescence

of a single fully mature and cAMP-bound yEPAC sensor molecule and a single fully mature and unbound yEPAC sensor molecule, respectively. These fluorescence values are fixed given an imaging setting. $[cAMP]$ is the concentration of cAMP, and K_d is the dissociation constant of cAMP binding to the FRET sensor (earlier determined to be $4 \mu M^{25}$).

$$\begin{aligned} \text{Corrected FRET ratio} &\equiv \frac{CFP_{sensor} - CFP_{mutant}}{RFP_{sensor}} \\ &= \frac{[cAMP] * (CFP_{S1} - CFP_m) + K_d * (CFP_{S2} - CFP_m)}{[cAMP] * RFP_{S1} + K_d * RFP_{S2}} \end{aligned} \quad 1$$

Here, although the partially mature species is no longer present, the subtraction has also introduced a new species, namely the fully matured species of the R279L mutant (CFP_m , Fig. 3B). This species cannot be bound by cAMP, and therefore its level of FRET between mTurquoise2 Δ and tdTomato remains constant. To determine the relation of the corrected FRET ratio and cAMP concentration, we need to know the relation of CFP_{S1} , CFP_{S2} , CFP_m in the numerator. In our experiments, we had observed that under the same conditions, the mutant strain has a higher FRET ratio (donor/acceptor) than the sensor strain (Fig. S5). A higher FRET ratio (donor/acceptor) suggests a relaxed state of the EPAC linker between the two fluorophores of the R279L mutant, since less energy is transmitted from the donor to the acceptor. Further, for the yEPAC sensor, when cAMP bound the EPAC linker, it relaxed the linker and increased the FRET ratio. Therefore, the R279L mutant resembles the cAMP bound state of the yEPAC sensor rather than the unbound state (namely, $CFP_m \sim CFP_{S1} > CFP_{S2}$). We therefore made an additional assumption that fluorescence value of the cAMP-bound yEPAC sensor is that same to that of the R279L mutant (namely, $CFP_m = CFP_{S1}$) (assumption 3). This allowed us to eliminate them from the equation, and derive equation 2:

$$\text{Corrected FRET ratio} = \frac{K_d * (CFP_{S2} - CFP_m)}{[cAMP] * RFP_{S1} + K_d * RFP_{S2}} \quad 2$$

Here, since $CFP_{S2} - CFP_m$ is negative, when $[cAMP]$ increases, the value of the right term in equation 2 also becomes larger (i.e., less negative). Therefore, by calculating the corrected FRET ratio from experimental data and with the above mentioned three assumptions, we can determine the change of cAMP during the cell cycle (on the populational-level) without knowing the single-molecule fluorescence values in equation 2.

Determination of cAMP dynamics during the cell cycle on different conditions

With the above reasoning and equation, we set out to determine the cAMP dynamics during the cell cycle when cells grew on glucose or acetate. For each condition, the sensor and the mutant strains were loaded into two microfluidic chips and imaged with identical imaging

conditions at the same time. To eliminate cell autofluorescence, wildtype YSBN6 cells (WT) were co-loaded into the chips and their autofluorescence in the CFP/RFP channels was determined and subtracted from the fluorescence of the sensor/mutant cells (Fig. S6). Cell cycles were segmented using the budding events, and only cell cycles with a normal duration (Fig. S7) were used for further analysis.

To calculate the corrected FRET ratio as in equation 1, we first aligned the selected cell cycles from budding to budding. We also set a minimal threshold (background corrected RFP > 5 a.u.) on the RFP fluorescence (autofluorescence subtracted) to exclude the cell cycles whose FRET sensor/mutant were expressed at a very low level and fluorescence intensity was indistinguishable from the background (after subtracting autofluorescence). We then calculated the mean CFP fluorescence at each time points for all the aligned cell cycles, for both the sensor and the mutant strain (Figure 4A, D), and likewise the mean RFP fluorescence for the sensor strain (Figure 4B, E), on glucose or acetate condition. From these values, we calculated the corrected FRET ratio at each time point following equation 1 (Figure 4C, F).

Here, we observed that on high glucose, the corrected FRET ratio during the cell cycle showed only subtle dynamics, suggesting that cAMP concentration remains mostly constant during the cell cycle, and perhaps somewhat higher at the budding than at the M phase (Figure 4C). On acetate, however, we observed oscillations with a larger amplitude that peak at budding, suggesting a higher cAMP concentration (Figure 4F). The observations on both glucose and acetate are consistent with the Msn2 localization patterns (plotted as dashed curve here, same as in Fig. 2B, D). Interestingly, since the corrected FRET ratio is a single-variable function of the cAMP concentration, it can be used to compare the cAMP concentration between cells grew in different nutrient conditions. Here too, we observed that on high glucose the corrected FRET ratio is consistently higher than that on acetate, suggesting a higher overall cAMP concentration when cells are growing on glucose. This result is consistent with our observations of the Msn2 localization pattern.

It is worth noting that for both glucose and acetate condition, the corrected FRET ratio at the beginning and the end of the cell cycle were not equal, and therefore it was not following a standard oscillation. This might be caused by some long-term accumulation of stress during the movie, such as the accumulation of photo-damage by CFP imaging, or aging. In fact, high expression of the FRET sensor could also be stressing the cells when grown on minimal medium, as the cell cycle duration on acetate is longer than what is normally observed for YSBN6 cells (260/270 minutes versus 200 minutes, Fig. S7)). Further optimization of experimental setting would be required to eliminate this effect.

In conclusion, cAMP concentration oscillates during the cell cycle when cells are grown on acetate. The peak of the oscillation appears at the time of budding, while the trough happens as the cell cycle progresses towards the end of mitosis. On glucose, no clear oscillation could be observed. These results are consistent with population data obtained earlier, where it was observed that synchronized elutriated cells cultivated on high glucose showed no clear cAMP oscillation, while for synchronized elutriated cells cultivated on glucose-limited condition (a condition resembling the poor nutrient source acetate) oscillations were observed, with peak and trough appearing at similar timepoints as our results¹⁰. Furthermore, the data also suggest that cAMP levels are overall higher when cells were grown on glucose, consistent with results obtained using *Msn2* as a cAMP/PKA reporter.

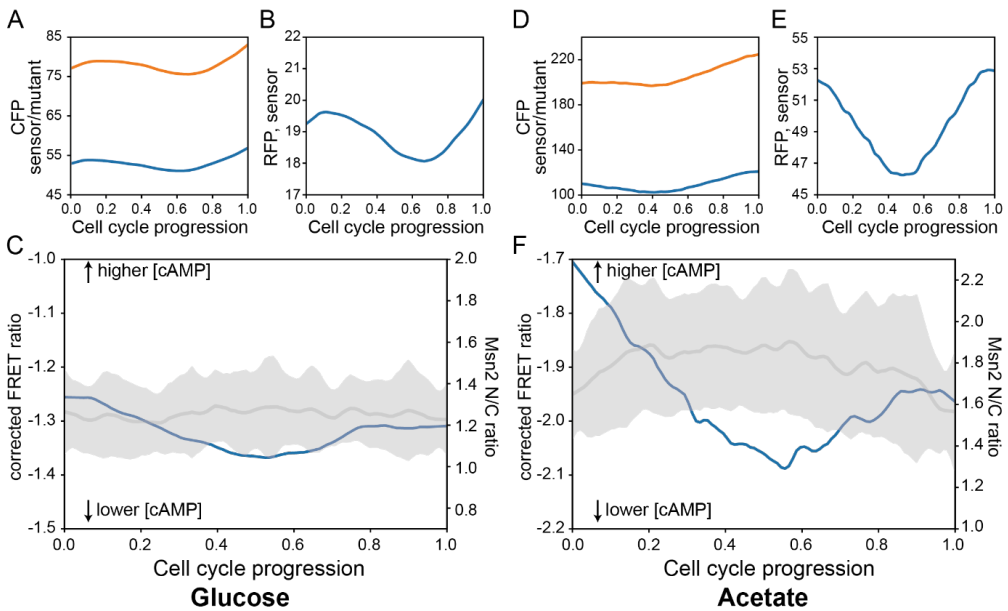


Fig. 4: cAMP concentration during the cell cycle, reported by FRET sensor. (A, B, D, E) All results shown were calculated after subtracting autofluorescence and filtering cell cycle with very low expression (RFP < 5 a.u.). (A) Mean CFP fluorescence calculated at each time point of the cell cycle, from 194 cell cycles of the sensor strain (blue) and 245 cell cycles of the mutant strain (orange), grown on glucose condition. (B) Mean RFP fluorescence calculated at each time point of the cell cycle from 194 cell cycles of the sensor strain, grown on glucose condition. (C) Blue line corresponding to the left axis is the corrected FRET ratio on high glucose, calculated using data in (A, B) and equation 1. Grey line corresponding to the right axis is the nucleus-to-cytosolic ratio of *Msn2*, same as shown in Fig. 2B, orange line. (D) Mean CFP fluorescence calculated at each time point of the cell cycle, from 99 cell cycles of the sensor strain (blue) and 103 cell cycles of the mutant strain (orange), grown on acetate condition. (E) Mean RFP fluorescence calculated at each time point of the cell cycle from 99 cell cycles of the sensor strain, grown on acetate condition. (F) Blue line corresponding to the left axis is the corrected FRET ratio on acetate, calculated using data in (D, E) and equation 1. Grey line corresponding to the right axis is the nucleus-to-cytosolic ratio of *Msn2*, same as shown in Fig. 2D, blue line.

cAMP/PKA activity gates early phase of cell cycle

When cells were grown on high glucose, our results above showed that cAMP concentration is rather constant, and therefore not coupled to the cell cycle oscillators. This suggests that cAMP concentration is not connected to the cell cycle oscillators, at least for this nutrient condition. Therefore, we asked if there is another role for cAMP concentration during the cell cycle. Towards this end, we controlled cAMP production during the cell cycle with auxin-based degradation of *Cyr1*, combined with optogenetically controlled bPAC activation. For each cell cycle, we recorded budding and cytokinesis. Here, after halting cAMP production with auxin, we observed that cells were no longer able to initiate a new cell cycle (i.e. produce a new bud) except for a few escapers (Fig. 5A). Interestingly, we observed that cells that have already budded were able to finish their current cell cycle, albeit with a much longer duration (Fig. 5B), suggesting that cAMP/PKA activity is essential for the initiation of a new cell cycle while also has function in the later cell cycle stages. This is consistent with previous result which shows that cells were halted after mitotic exit after depleting *Cyr1* with auxin, by using NAD(P)H oscillations as a cell cycle phase indicator³². To confirm that the effect observed is indeed caused by cAMP depletion, we reactivated cAMP production with constant blue light and bPAC. Cells were able to initiate cell cycles with normal cell cycle durations when sufficient amount of light was given (Fig. 5C). This suggests that a high cAMP concentration is gating the early phase of the cell cycle on glucose. Since cAMP concentration also rise during the early cell cycle on acetate (Fig. 2C, 2D; Fig. 4F), we expect to see a similar effect on acetate, although this remains to be tested.

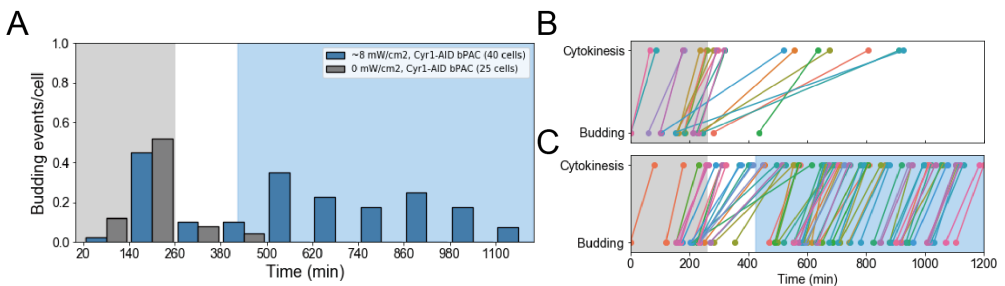


Fig. 5: cAMP gates the early phase of cell cycle. (A) The number of budding events per cell every two hours throughout the movie represents how well the population is growing. Grey shading represents the period where no auxin nor light were applied. The white shading represents the period where auxin was added to both population; the blue shading represents the period where auxin remained added to both population, and cells in one field of view were illuminated by blue light (blue column) while the rest of cells remained in the dark (grey columns). (B) Cell cycles from cells with *Cyr1* depletion by auxin and remained in the dark were depicted as slanted lines that connect the time point of budding and cytokinesis. Shading is the same as in (A). When *Cyr1* was depleted by auxin (white shading), 11 cell cycles that had budded were able to reach cytokinesis, 2 cell cycles that had budded were not able to reach cytokinesis (not shown). New cell cycles cannot be initiated, with 2 exceptions in which *Cyr1* might not be fully depleted or might have passed START when *Cyr1* was depleted. (C) Cell cycles from cells with *Cyr1* depletion by auxin and after 3 hours were illuminated by blue light of 8 mW/cm² were depicted as slanted lines. By blue light illumination, new cell cycles can be initiated again with a normal cell cycle duration as seen by the slope of the lines.

Discussion

In this work, we determined for the first time the dynamics of cAMP concentration during the cell cycle in single cells. We established two different methods for this purpose, namely the use of Msn2 localization and a FRET sensor with corrected FRET ratio, and quantified cAMP concentrations on glucose and acetate. Both methods yielded similar results, revealing a consistently high level of cAMP concentration in cells grown on glucose, and lower levels on acetate, which also displayed oscillations. We further developed a method that combines inducible protein degradation with optogenetics for controlling cellular cAMP production on single cell level, and provided evidence that cAMP gates the initiation of a new cell cycle.

To estimate cAMP concentration using single-cell FRET sensor data, we made three assumptions in order to calculate a corrected FRET ratio (Fig. 3C, supplementary method 1). However, whether these assumptions are fully solid requires further investigation. First, regarding assumption 1 (same expression pattern in the mutant and sensor strains), the expression of the FRET sensor/mutant from a genomically-integrated cassette should be preferred for future experiments, as it will reduce the variability of expression levels within each strain, and therefore consolidate this assumption. Second, assumption 2 (no cross-excitation of RFP) might require further examination, since the extinction coefficient of tdTomato at the CFP excitation wavelength (438 nm) is not negligible (Fig. S4A). However, since this only concerns the partially mature species with mature tdTomato, which is expected to be presented at a lower abundance (since tdTomato has a longer maturation time than mTurquoise2), assumption 2 is likely valid. Finally, the actual values of CFP_{s1} and CFP_m have not been experimentally determined. If assumption 3 (equation 10) does not hold, then the relationship of the corrected FRET ratio and cAMP concentration is unclear, and will depend on the sign of the numerator of equation 9. In this case, the fluorescence value of a single sensor/mutant molecule (CFP_{s1} , CFP_m , CFP_{s2} , CFP_m , RFP_{s1} , RFP_{s2}) should be experimentally determined. This could be achieved *in vitro* with purified and fully matured sensor/mutant molecules. In fact, by using these values and equation 1, we could perform absolute quantification of cAMP concentration over time.

This work has assembled a comprehensive toolset for studying the cAMP/PKA pathway. By combining the tools presented here, one could achieve a more in-depth understanding of cAMP/PKA function in the future. As an example, one could control the cAMP synthesis rate by using different light dosages for bPAC activation after depleting Cyr1 with auxin. If at the same time, one would also measure the cAMP concentration using the FRET sensor, it would be possible to determine the relation between blue light dosage and cAMP concentration. One potential problem here is that both bPAC activation and the yEPAC sensor measurement

require blue light. However, bPAC activation requires weak illumination (e.g., 4 mW/cm²) on the minute timescale, while FRET sensor activation requires strong illumination (e.g., 100 mW/cm²) on the millisecond timescale. Therefore, the two applications should be compatible. With this fine control and measurement, one could answer questions such as what level of cAMP concentration is necessary for a cell to enter the cell cycle.

We have shown that, although cAMP concentration is rather constant during the cell cycle in cells grown on high glucose, it is most essential for the early phase. A plausible explanation for this observation is that depletion of cAMP causes hyper-activity of Msn2, a condition similar to the overexpression of a constitutively active allele of Msn2 (Msn2A6)³³, which causes cell cycle arrest at the G₁/S transition. Indeed, all PKA kinases (TPK1/2/3) become dispensable when Msn2 and Msn4 are deleted³⁴. However, the exact mechanism of cell cycle arrest by Msn2 activity is not fully clear³³. Yet another mechanism that could explain the essentiality of PKA could be the function of PKA in promoting expression of Cln3 through inhibition of Whi3³⁵. By phosphorylating Whi3 on Ser-568, PKA releases the mRNA of Cln3 and promotes the onset of START³⁵. A S568A mutation on Whi3 led to prolonged G₁ duration and decelerated Cln2 transcription³⁵. For the rest of the cell cycle on glucose condition, cAMP/PKA might have some other functions, since depletion of cAMP extend the duration of the cell cycle that has already initiated.

On acetate, cAMP concentration increases during the early cell cycle, peaks around budding and decreases afterwards. The rising cAMP concentration during the early cell cycle validates the important role of cAMP/PKA in cell cycle initiation. Also, it is interesting to ask, why does cAMP oscillate on acetate, but not on glucose? One explanation is that the mechanism that cause cAMP oscillation is present in both nutrient conditions, but cAMP oscillation is masked when cells are growing on glucose, due to constant signalling from the environment^{6,7} or constantly high glycolytic flux⁹. Such mechanism could be an oscillating concentration of the guanine nucleotide exchange factor Cdc25. Cdc25 contains a cyclin-destruction box similar to the mitotic cyclins, and could be regulated via ubiquitin-dependent degradation³⁶. Since Cdc25 also promotes adenylate cyclase activity through Ras1/2³⁷, its accumulation in G₁ phase and later degradation (due to change in ubiquitin-ligase activity) could explain the oscillation of cAMP/PKA level. Alternatively, since the oscillation of cAMP concentration largely overlaps with the oscillation of NAD(P)H, it could also be driven by the metabolic oscillator underlying NAD(P)H oscillation. An alternative explanation is that the mechanism that cause cAMP oscillation is only present when cells are growing on acetate. For example, certain metabolic pathways, such as glycolysis, could be oscillating only on acetate, and such oscillation could be sensed by cAMP/PKA pathways. Overall, the origin and function of cAMP oscillation require further investigation.

How signalling pathways could participate in cell cycle regulation is a less-studied topic. However, as signalling pathways are able to control cell growth in response to environmental signals, they could also play a role in cell cycle control in a constant environment by receiving signals from intracellular sources. The PKA pathway, for example, could be regulated by FBP⁹. The observed oscillation of cAMP concentration on acetate, as well as the toolset assembled in this study, are therefore the starting point for dissecting the role of cAMP/PKA in cell cycle regulation. Combining perturbations on and readouts of the cell cycle machinery and metabolic oscillator, should aid in achieving this goal in the future.

Acknowledgements

Funding from the following sources is acknowledged: the Chinese Scholarship Council (for H.C.). We would like to thank Bas Teusink, Kees Jalink and Dennis Botman for sharing the plasmids and information regarding the yEPAC sensor.

Author contribution

Conceptualization: HC, MH; Experiment and data analysis: HC, SJ, EC; Derivation of the corrected FRET ratio: HC; Writing: HC; Revision: HC, MH, AM; Supervision: MH, AM. Funding acquisition: MH, HC; Project administration: MH.

Materials and method

Strains and strain construction

Yeast strains used in this study are based on the S288c-derived strains YSBN6 (prototrophic) or YSBN10 (auxotrophic, *ura3-*). All cloning efforts were performed using the MoClo YTK protocol³⁸, which had been adapted for CRISPR-Cas9 genome editing. In order to track Msn2 localization state, we tagged the transcription factor with the fluorescent proteins mVenus or tdGFP. To enable dynamic depletion of the adenylate cyclase *Cyr1*, we tagged *Cyr1* with the truncated degron sequence AID⁷¹⁻¹¹⁴, the usage of which has been established and applied in yeast cells previously^{17,18}. For the constitutive expression of bacterial photoactivatable adenylate cyclase bPAC, we integrated the bPAC sequence into the X1 locus at chromosome X of the yeast genome³⁹. To visualize the nucleus, the histone H2A is tagged with a mRFP1. Yeast transformations were performed according to the lithium acetate high-efficiency protocol⁴⁰. Correct integration of all constructs into each host strain was verified using PCR and subsequently Sanger sequencing by Eurofins Genomics Mix2SeqON. Refer to supplementary table S1 for an overview on developed and/or used yeast strains, and to supplementary table S2 for primer sequences used for the development thereof.

Cell cultivation and microfluidics

For the pre-culture in glucose medium, single colonies from YPD 20 g/L glucose agar plates were picked and inoculated in 10 mL YNB 2% glucose medium in 100 mL Erlenmeyer flasks, then grown for 8 hours in the shaker (30 C, 300 rpm). The culture was then used for the first re-inoculation in a fresh, pre-warmed 10 mL YNB 2% glucose medium to grow overnight to an OD between 1 and 1.5. The exponentially growing culture was finally used

for the second re-inoculation and diluted in pre-warmed 10 mL YNB 2% glucose medium to an OD of 0.05 and grown to an OD of 0.08 to 0.15 (~3 hours incubation) which is suitable for loading of cells into the microfluidic device. For the results in Figure 1 and Figure S1, cells were cultured using the Verduyn minimal medium⁴¹ instead of YNB.

For the pre-culture in acetate medium, single colonies from YPD 20 g/L glucose agar plates were picked and inoculated in 10 mL YPD medium in 100 mL Erlenmeyer flasks, then grown for ~15 hours in the shaker (30 C, 300 rpm), until the culture reached stationary phase (around OD=20.0). YPD was completely removed by the culture after spinning down cells by centrifugation (30 C, 3900 rpm, 4 minutes). Then, as a washing step to fully remove residual YPD, the culture was resuspended with YNB 1% acetate (calculated without the sodium ion weight) and again spun down using centrifugation (30 C, 3900 rpm, 4 minutes). Finally, the culture was resuspended in YNB 1% acetate and re-inoculated in fresh, pre-warmed YNB 1% acetate to an OD of 0.0125 and grown for about 24~30 hours (4 to 5 generation plus adaptation lag time). The exponentially growing culture was used for a third re-inoculation in pre-warmed 10 mL YNB 1% acetate medium and grown for another 3~4 generations (~15 hours), reaching an OD of 0.08 to 0.15 for loading. Overall, OD of the acetate flask culture was kept below 0.7 to maintain an exponential growing culture.

When the culture has reached a state suited for microfluidic experiments, it was used to load to the microfluidic chip according to protocol⁴². Throughout microfluidic experiments, the cells receive the designated fresh, pre-warmed medium. Flow rate for the glucose condition was 4.8 $\mu\text{L}/\text{min}$ while flow rate for the acetate condition was 4 $\mu\text{L}/\text{min}$. In all experiments with *Cyr1*-AID depletion, the respective *Cyr1*-AID strain was simultaneously loaded with cells expressing mGFP-AID (YSBN6.G2J), in 5:1 ratio, in order to pinpoint the moment of depletion of all AID-fused proteins. To deplete the degron-tagged proteins, the medium was switched to pre-warmed medium containing 0.1 mM of NAA (synthetic auxin, naphthalene-acetic acid) by manually reconnecting the inlet tubing to a different syringe.

Microscopy

For image acquisition, a Nikon Ti-E inverted microscope was used, equipped with an Andor iXon Ultra 897 EM-CCD camera, the Nikon PFS dynamic focusing system, a 100x Nikon Super Fluor Apochromat objective, and a Lumencor Light Engine Aura II 4-LCR-XA or a CoolLed pE2 light excitation system. Bright field images were obtained using a halogen lamp as a light source, and an ultraviolet (420 nm beam-splitter) and FEO600 (600 nm beam-splitter) light filter was used to filter its light to minimize cell damage during the long image acquisition. The frequency of acquisition used depends on the culture imaged: glucose cultures have been imaged every 5 minutes, while acetate cultures have been imaged every 10 minutes. To exclude stress effects due to the loading into the

microfluidic device, cells loaded in the microscope have been kept in the dark 2-2.5 hours in case of glucose culture and 3-3.5 hours in case of acetate culture before imaging starts. For GFP imaging, the GFP channel of the Lumencor Light Engine Aura II 4-LCR-XA was set at 3% power, with an exposure time of 200 ms. For mRFP1 imaging, the RFP channel of the Lumencor Light Engine Aura II 4-LCR-XA was set at 3% with an exposure time of 300 ms. For mVenus imaging, the YFP channel of the CoolLed pE2 was set at 20% power, with an exposure time of 500 ms and an increased camera gain (gain 3) to enhance visibility of localization. For FRET imaging, a Nikon Ti-E inverted microscope equipped with a dual-camera dual-filter-turret system was used. Filter set used was depicted in Fig. S4B. For excitation of the FRET pair, the CFP channel of the CoolLed pE2 was set at 10% power, with an exposure time of 100 ms.

FRET sensor testing by adding glucose

For the pyruvate to glucose nutrient switching experiment that tested the FRET sensor, cells cultured in Verduyn minimal medium with 10 g/L pyruvate were immobilized on Concanavalin A (ConA) modified μ -Slide (ibidi 80821). Notably, the cells used in this experiment were switched from a culture in Verduyn minimal medium with high glucose into pyruvate. Perhaps due to the unsuccessful switch, the cells were barely growing on pyruvate. Nevertheless, we used it as glucose-deprived cells to test the FRET sensor by adding glucose. For coating, 250 μ L of 1 mg/mL ConA was added per well and left for 10 minutes. The ConA solution was subsequently removed and the well was washed with 200 μ L sterile MiliQ. The well was then left for drying for 20 minutes. For loading, 300 μ L of cells at OD=0.1 was added and incubated at 30 degrees for 30 minutes in resting. After that, residual cells were removed and the well was washed with 300 μ L pre-warmed medium. Then, another 300 μ L of pre-warmed medium was added to the well, and the slide was ready for imaging.

Before adding glucose, images were taken at one frame per five minutes frequency for about 45 minutes. To switch cells into high glucose, 10 μ L of 600 g/L glucose stock was gently added to the wells, and imaging was immediately started at a one frame per 30 seconds frequency to enable capturing of the fast response of cAMP. Ideally, glucose should be added right after obtaining the previous frame (on acetate). However, in this experiment there was a five minutes waiting time. Given that the FRET ratio before adding glucose was rather stable, this waiting time (where no data was obtained) was removed during the analysis. The yEPAC sensor strain and the yEPAC-R279L mutant strain were tested separately to minimize the waiting time caused by perturbation.

Optogenetics

To perturb cells with blue light, we used a multiwavelength patterned illuminator (Polygon400, Mightex) integrated into the microscope, at a wavelength of 455 nm with all pixels on. The Polygon illumination shared the light path of DIC channels, with a ND filter installed to reduce the light intensity by 1000-fold. The polygon was controlled by independent software from the microscope, and was manually switched on and off when time control was needed. To constantly illuminate a target field of view while keeping other filter views in dark, we kept the polygon constantly on, and set the combination of the target field of view with the DIC channel as the last point (i.e., rest position between imaging) in the microscope job queue. The blue light intensity of the polygon (as used in Fig. 5, A, C) was measured by a Thorlab light sensor (S120VC) at the sample specimen.

Data analysis

For pre-processing of the microscopy images, a macro was used in ImageJ⁴³ to enhance contrast and sharpen the DIC image. The images were then passed to a Python 2.7 script for further processing. First, fluorescence images were background subtracted by subtracting the camera baseline (500 a.u.). In the fluorescence channels, illumination intensity and therefore fluorescence output might be slightly weaker at the edges of each position. To correct for this uneven illumination effect and make the field of view ‘flat’, for every fluorescent channel we stacked images from a selected frame across all field of views, and obtained the median intensity for every pixel, which removed objects such as cells and yielded a background image. A Gaussian fit was performed on this background image for smoothing. Next, for every pixel, the ratio of the pixel intensity to the maximal pixel intensity of the smoothed background image was calculated, which together composed a flat field correction matrix. To apply this correction process, every fluorescent image was subtracted by the camera baseline and then multiplied with the corresponding correction matrix. Furthermore, the 10th percentile of this corrected image was used as the background fluorescent (e.g., emitted by medium) and subtracted from the images.

In the FRET sensor imaging, the dual camera system was not well perfectly aligned. Since the cell segmentation (see below) was performed in the brightfield, fluorescent channels that were misaligned to the brightfield needed correction. To do so, we used the StackReg function from the Python package pystackreg, with the RIGID_BODY method to register different channels. Notably, the RFP channel was taken from the same camera as the brightfield and well aligned (Fig. S8), we used it as a reference, because it had a similar pixel intensity level as other fluorescent channel. If a channel’s intensity values were significantly higher than the other, then it could be scaled down by dividing with the average fold difference.

For cell segmentation and tracking, the BudJ plug-in⁴⁴ for ImageJ was used to segment and track single yeast cells. Specifically, cells to segment were selected at their centre in the DIC image, and cell boundaries were estimated by BudJ based on an 8% change in contrast at the perimeter of the cell. Budding and cytokinesis timepoints were manually determined using the first moment of bud appearance on the cell surface, and moment of forward projecting of the daughter cell, respectively. The BudJ segmentation yielded parameters for an ellipse as the segmented cell shape, which were passed to a Python 2.7 script. In the script, an ellipsoid mask was created using these parameters to obtain values of each pixel within the segmented cell.

For data analysis of Msn2 localization when using Hta2-mRFP1 as a nucleus marker, we determined the center of the nucleus in the RFP channel by taking the center of mass, and segmented a circular area using this center which has a radius of 3 pixels. This circular area is used to calculate the nucleus GFP intensity in the GFP channel. Another circular area with the same center and a radius of 9 pixels is also segmented, and cellular pixels out of this area were considered cytoplasmic. Then we computed the ratio between the average GFP intensity of nuclear pixels and the average intensity of the cytosolic pixels.

To align cell cycles for data analysis of Msn localization, cell cycles with a normal duration (between 50 and 200 minutes for glucose cultures and between 100 and 300 minutes for acetate cultures), were spliced using the time of two consecutive budding events. The datapoints (around 20-30, including the first budding but not the second budding) for these cell cycles were converted to relative time by fitting a one-dimensional linear spline (without smoothing) through the original data and retrieving 100 datapoints with equal time interval from this spline. The time interval of the cell cycle duration was then replaced with [0,1).

In the FRET experiments, WT cells were co-loaded to correct for cellular auto-fluorescence in both the CFP and RFP channel. They were differentiated from either the sensor strain or mutant strain as shown in Fig. S6. For auto-fluorescence correction, the median fluorescence intensity (CFP/RFP) of WT cells throughout the movie was calculated and subtracted from each single cell of the sensor/mutant strain.

Reference

1. Papagiannakis, A., Niebel, B., Wit, E. C. & Heinemann, M. Autonomous Metabolic Oscillations Robustly Gate the Early and Late Cell Cycle. *Mol. Cell* **65**, 285–295 (2017).
2. Takhaviev, V. Dissecting the temporal dynamics of eukaryotic metabolism in single cells. (University of Groningen, 2020). doi:10.33612/diss.119793412
3. Özsezen, S. *et al.* Inference of the High-Level Interaction Topology between the Metabolic and Cell-Cycle Oscillators from Single-Cell Dynamics. *Cell Syst.* **9**, 354–365.e6 (2019).
4. Orlando, D. A. *et al.* Global control of cell-cycle transcription by coupled CDK and network oscillators. *Nature* **453**, 944–7 (2008).
5. Simmons Kovacs, L. A., Orlando, D. A. & Haase, S. B. Transcription networks and cyclin/CDKs: the yin and yang of cell cycle oscillators. *Cell Cycle* **7**, 2626–2629 (2008).
6. Zaman, S., Lippman, S. I., Zhao, X. & Broach, J. R. How *Saccharomyces* responds to nutrients. *Annu. Rev. Genet.* **42**, 27–81 (2008).
7. Dechant, R., Saad, S., Ibáñez, A. J. & Peter, M. Cytosolic pH regulates cell growth through distinct GTPases, Arf1 and Gtr1, to promote Ras/PKA and TORC1 activity. *Mol. Cell* **55**, 409–421 (2014).
8. Kochanowski, K. *et al.* Functioning of a metabolic flux sensor in *Escherichia coli*. *Proc. Natl. Acad. Sci. U. S. A.* **110**, 1130–1135 (2013).
9. Peeters, K. *et al.* Fructose-1,6-bisphosphate couples glycolytic flux to activation of Ras. *Nat. Commun.* **8**, 922 (2017).
10. Müller, D., Exler, S., Aguilera-Vázquez, L., Guerrero-Martín, E. & Reuss, M. Cyclic AMP mediates the cell cycle dynamics of energy metabolism in *Saccharomyces cerevisiae*. *Yeast* **20**, 351–367 (2003).
11. Futcher, B. Metabolic cycle, cell cycle, and the finishing kick to Start. *Genome Biol.* **7**, 107 (2006).
12. Zhao, G., Chen, Y., Carey, L. & Futcher, B. Cyclin-Dependent Kinase Co-Ordinates Carbohydrate Metabolism and Cell Cycle in *S. cerevisiae*. *Mol. Cell* **62**, 546–557 (2016).
13. Ewald, J. C., Kuehne, A., Zamboni, N. & Skotheim, J. M. The Yeast Cyclin-Dependent Kinase Routes Carbon Fluxes to Fuel Cell Cycle Progression. *Mol. Cell* **62**, 532–545 (2016).
14. van Heerden, J. H. *et al.* Lost in Transition: Start-Up of Glycolysis Yields Subpopulations of Nongrowing Cells. *Science (80-)*. **343**, 1245114–1245114 (2014).
15. Görner, W. *et al.* Nuclear localization of the C2H2 zinc finger protein Msn2p is regulated by stress and protein kinase A activity. *Genes Dev.* **12**, 586–597 (1998).
16. Nishimura, K., Fukagawa, T., Takisawa, H., Kakimoto, T. & Kanemaki, M. An auxin-based degron system for the rapid depletion of proteins in nonplant cells. *Nat. Methods* **6**, 917–922 (2009).
17. Morawska, M. & Ulrich, H. D. An expanded tool kit for the auxin-inducible degron system in budding yeast. *Yeast* **30**, 341–351 (2013).
18. Papagiannakis, A., De Jonge, J. J., Zhang, Z. & Heinemann, M. Quantitative characterization of the auxin-inducible degron: A guide for dynamic protein depletion in single yeast cells. *Sci. Rep.* **7**, 1–13 (2017).
19. Stierl, M. *et al.* Light modulation of cellular cAMP by a small bacterial photoactivated adenylyl cyclase, bPAC, of the soil bacterium *Beggiatoa*. *J. Biol. Chem.* **286**, 1181–1188 (2011).
20. Stewart-Ornstein, J., Chen, S., Bhatnagar, R., Weissman, J. S. & El-Samad, H. Model-guided optogenetic study of PKA signaling in budding yeast. *Mol. Biol. Cell* **28**, 221–227 (2017).
21. Cai, L., Dalal, C. K. & Elowitz, M. B. Frequency-modulated nuclear localization bursts coordinate gene regulation. *Nature* **455**, 485–490 (2008).

22. Logg, K., Bodvard, K., Blomberg, A. & Käll, M. Investigations on light-induced stress in fluorescence microscopy using nuclear localization of the transcription factor Msn2p as a reporter. *FEMS Yeast Res.* **9**, 875–884 (2009).
23. El Najjar, N. *et al.* Bacterial cell growth is arrested by violet and blue, but not yellow light excitation during fluorescence microscopy. *BMC Mol. cell Biol.* **21**, 35 (2020).
24. De Wever, V., Reiter, W., Ballarini, A., Ammerer, G. & Brocard, C. A dual role for Pp1 in shaping the Msn2-dependent transcriptional response to glucose starvation. *EMBO J.* **24**, 4115–4123 (2005).
25. Botman, D. *et al.* A yeast FRET biosensor enlightens cAMP signalling. *Mol. Biol. Cell* mbcE20050319 (2021). doi:10.1091/mbc.E20-05-0319
26. Canelas, A. B. *et al.* Integrated multilaboratory systems biology reveals differences in protein metabolism between two reference yeast strains. *Nat. Commun.* **1**, 145 (2010).
27. Ponsioen, B. *et al.* Direct spatial control of Epac1 by cyclic AMP. *Mol. Cell. Biol.* **29**, 2521–2531 (2009).
28. Alon, U. *An Introduction to Systems Biology: Design Principles of Biological Circuits.* (CRC Press, 2019).
29. Balleza, E., Kim, J. M. & Cluzel, P. Systematic characterization of maturation time of fluorescent proteins in living cells. *Nat. Methods* **15**, 47–51 (2018).
30. Liu, B. *et al.* Influence of Fluorescent Protein Maturation on FRET Measurements in Living Cells. *ACS sensors* **3**, 1735–1742 (2018).
31. Russell, M., Bradshaw-Rouse, J., Markwardt, D. & Heideman, W. Changes in gene expression in the Ras/adenylate cyclase system of *Saccharomyces cerevisiae*: correlation with cAMP levels and growth arrest. *Mol. Biol. Cell* **4**, 757–765 (1993).
32. Papagiannakis, A. Intrinsic, periodic and tunable metabolic dynamics: a scaffold for cellular coherence. (University of Groningen, 2017).
33. Pfanzagl, V. *et al.* A constitutive active allele of the transcription factor Msn2 mimicking low PKA activity dictates metabolic remodeling in yeast. *Mol. Biol. Cell* **29**, 2848–2862 (2018).
34. Smith, A., Ward, M. P. & Garrett, S. Yeast PKA represses Msn2p/Msn4p-dependent gene expression to regulate growth, stress response and glycogen accumulation. *EMBO J.* **17**, 3556–3564 (1998).
35. Mizunuma, M. *et al.* Ras/cAMP-dependent protein kinase (PKA) regulates multiple aspects of cellular events by phosphorylating the Whi3 cell cycle regulator in budding yeast. *J. Biol. Chem.* **288**, 10558–10566 (2013).
36. Kaplon, T. & Jacquet, M. The cellular content of Cdc25p, the Ras exchange factor in *Saccharomyces cerevisiae*, is regulated by destabilization through a cyclin destruction box. *J. Biol. Chem.* **270**, 20742–20747 (1995).
37. Mintzer, K. A. & Field, J. The SH3 domain of the *S. cerevisiae* Cdc25p binds adenylyl cyclase and facilitates Ras regulation of cAMP signalling. *Cell. Signal.* **11**, 127–135 (1999).
38. Lee, M. E., DeLoache, W. C., Cervantes, B. & Dueber, J. E. A Highly Characterized Yeast Toolkit for Modular, Multipart Assembly. *ACS Synth. Biol.* **4**, 975–986 (2015).
39. Mikkelsen, M. D. *et al.* Microbial production of indolyglucosinolate through engineering of a multi-gene pathway in a versatile yeast expression platform. *Metab. Eng.* **14**, 104–111 (2012).
40. Gietz, R. D. & Schiestl, R. H. High-efficiency yeast transformation using the LiAc/SS carrier DNA/PEG method. *Nat. Protoc.* **2**, 31–34 (2007).
41. Verduyn, C., Postma, E., Scheffers, W. A. & Van Dijken, J. P. Effect of benzoic acid on metabolic fluxes in yeasts: a continuous-culture study on the regulation of respiration and alcoholic fermentation. *Yeast* **8**, 501–517 (1992).
42. Huberts, D. H. E. W. *et al.* Construction and use of a microfluidic dissection platform for long-term imaging of cellular processes in budding yeast. *Nat. Protoc.* **8**, 1019–27 (2013).

43. Schneider, C. A., Rasband, W. S. & Eliceiri, K. W. NIH Image to ImageJ: 25 years of image analysis. *Nat. Methods* **9**, 671–675 (2012).
44. Ferrezuelo, F. *et al.* The critical size is set at a single-cell level by growth rate to attain homeostasis and adaptation. *Nat. Commun.* **3**, 1012 (2012).

Supplemental Information for Chapter 4

The dynamics and functions of the second-messenger cAMP during the yeast cell cycle

4

Haoqi Chen, Suzanne Jansen, Enrico Calzati, Andreas Miliadis-Argeitis, Matthias Heinemann

1 Molecular Systems Biology, Groningen Biomolecular Sciences and Biotechnology Institute, University of Groningen, Nijenborgh 4, 9747 AG Groningen, The Netherlands

* Lead Contact: Phone: +31 50 363 8146, Twitter: @HeinemannLab, E-mail: m.heinemann@rug.nl

Supplementary Text

FRET data analysis

To derive on the populational level a corrected FRET ratio which is determined by cAMP concentration and not affected by the partially mature species, we used fluorescence from the yEPAC-R279L mutant strain. As shown in Fig. 3B, several sensor species exist in each strain. We assumed that the sensor and the mutant strains have the same expression pattern (assumption 1), and used M to represent the (averaged) total number of fully-matured sensor/mutant molecules in a single cell. We also used M_1 to represent the number of matured and cAMP-bound sensor molecules, and M_2 to represent the number of matured and unbound sensor molecules. Therefore:

$$M \equiv M_1 + M_2 \quad 1$$

Further, we used N to represent the (averaged) total number of partially mature sensor or mutant molecules (from here on, the partially mature species always refers to a species with a matured mTurquoise2 Δ and an immature tdTomato). We also used CFP_{s1} or CFP_{s2} to represent the CFP fluorescence of a single fully-matured sensor molecule in the cAMP-bound or unbound state, CFP_m to represent the CFP fluorescence of a single fully-matured mutant molecule, CFP_{un} to represent the CFP fluorescence of a single partially mature sensor or mutant species. Therefore, the averaged CFP fluorescence that is measured experimentally in a single cell of the sensor strain is:

$$CFP_{sensor} = M_1 * CFP_{s1} + M_2 * CFP_{s2} + N * CFP_{un} \quad 2$$

And the averaged CFP fluorescence that is measured experimentally in a single cell of the mutant strain is:

$$CFP_{mutant} = M * CFP_m + N * CFP_{un} \quad 3$$

Similarly, we used RFP_{s1} or RFP_{s2} to represent the RFP fluorescence of a single fully-matured sensor molecule in the cAMP-bound or unbound state. We assumed that there is no cross-excitation of tdTomato by the CFP excitation light (assumption 2), and therefore the averaged RFP fluorescence that is measured in a single cell of the sensor strain is:

$$RFP_{sensor} = M_1 * RFP_{s1} + M_2 * RFP_{s2} \quad 4$$

With the above definition, we considered the following term:

$$\text{Corrected FRET ratio} \equiv \frac{CFP_{\text{sensor}} - CFP_{\text{mutant}}}{RFP_{\text{sensor}}} \quad 5$$

Here, by using Equation 2, 3 and 4, we obtained:

Corrected FRET ratio

$$\begin{aligned} &= \frac{(M_1 * CFP_{S1} + M_2 * CFP_{S2} + N * CFP_{un}) - (M * CFP_m + N * CFP_{un})}{M_1 * RFP_{S1} + M_2 * RFP_{S2}} \quad 6 \\ &= \frac{M_1 * CFP_{S1} + M_2 * CFP_{S2} - M * CFP_m}{M_1 * RFP_{S1} + M_2 * RFP_{S2}} \end{aligned}$$

Here, note that the effect of the partially mature species has been eliminated. By further using Equation 1, we obtained:

Corrected FRET ratio

$$\begin{aligned} &= \frac{M_1 * CFP_{S1} + M_2 * CFP_{S2} - M_1 * CFP_m - M_2 * CFP_m}{M_1 * RFP_{S1} + M_2 * RFP_{S2}} \quad 7 \\ &= \frac{M_1 * (CFP_{S1} - CFP_m) + M_2 * (CFP_{S2} - CFP_m)}{M_1 * RFP_{S1} + M_2 * RFP_{S2}} \end{aligned}$$

Since cAMP concentration would affect the ratio of bound versus unbound fully-matured sensor molecules, we introduced the following term:

$$\beta = M_1/M_2 \quad 8$$

Here, when cAMP concentration increases, β will also increase. By applying equation 8 in equation 7, we obtained:

$$\text{Corrected FRET ratio} = \frac{\beta * (CFP_{S1} - CFP_m) + (CFP_{S2} - CFP_m)}{\beta * RFP_{S1} + RFP_{S2}} \quad 9$$

The dissociation constant of the yEPAC sensor has been measured to be $4 \mu\text{M}^1$. Since EPAC, the part of the FRET sensor that binds cAMP, has only one binding site^{2,3}, we have the following:

$$K_d = \frac{[\text{cAMP}] * M_2}{M_1} \quad 10$$

And by substituting with equation 8, we have:

$$\beta = \frac{1}{K_d} * [\text{cAMP}] \quad 11$$

Therefore:

$$\text{Corrected FRET ratio} = \frac{[\text{cAMP}] * (CFP_{S1} - CFP_m) + K_d * (CFP_{S2} - CFP_m)}{[\text{cAMP}] * RFP_{S1} + K_d * RFP_{S2}} \quad 12$$

Here, we assumed that the fluorescence value of the cAMP-bound sensor (in which FRET effect is reduced) is the same as the mutant molecule (in which cAMP cannot be bound and a reduced FRET effect has been observed, Fig. S5) (assumption 3):

$$CFP_{S1} = CFP_m \quad 13$$

and obtained:

$$\text{Corrected FRET ratio} = \frac{K_d * (CFP_{S2} - CFP_m)}{[\text{cAMP}] * RFP_{S1} + K_d * RFP_{S2}} \quad 14$$

or equation 2 in the main text.

In theory, due to FRET effect CFP_{S2} is smaller than CFP_{S1} or CFP_m . Therefore, according to equation 11, the corrected FRET ratio should be a negative value. Indeed, when calculated with experimental data according to the definition in equation 5, the corrected FRET ratio was a negative value as shown in Fig. 4C, F. Therefore, when cAMP concentration increases, the corrected FRET ratio will also increase. Thus, the corrected FRET ratio is a good indicator of cAMP concentration under the above (three) assumptions.

Supplemental Figures

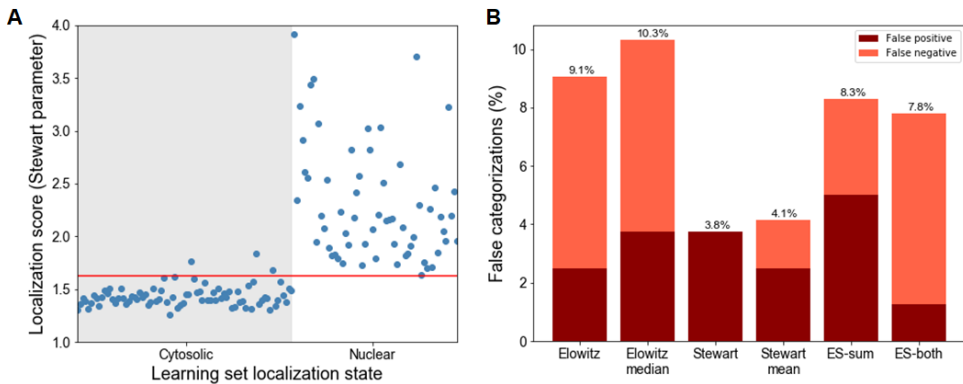


Fig. S1: Optimization of localization parameters and thresholding. (A). Determining an optimized threshold of a given parameter (S-parameter in this case). For each experiment, a learning set was manually assigned that contains single cells at certain frames with either nuclear or cytosolic Msn2 localization. Localization scores were then calculated for each data point and plotted. Shown here on the left are all S-parameter scores with cytosolic Msn2 localization, and on the right are all scores with nuclear Msn2 localization. A threshold (red line) was then determined that categorize events as cytosolic (localization score lower than threshold) or nuclear (localization score higher than threshold). When optimized, the threshold would minimize the amount of falsely assigned data points (false categorizations). (B). Performance comparison of each localization parameters. For explanation of how each parameter was computed, see Table S3. Parameter with the lowest sum of both false positive and false negative (S-parameter) was selected for further application.

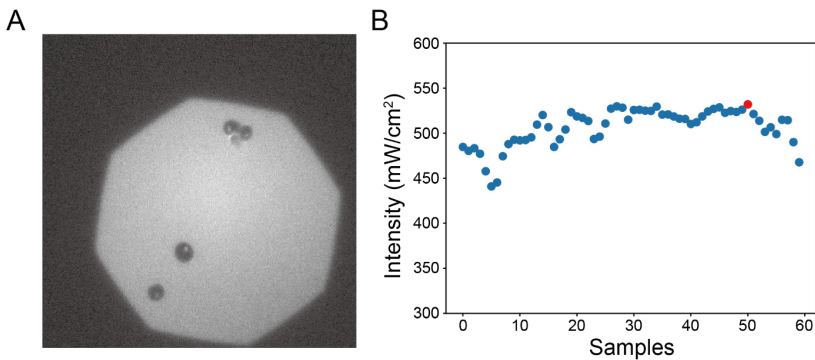


Fig. S2: Light intensity measurements and toxicity estimation. (A). A pinhole set in the light path of the microscope was used to constrain the shape of the light beam, so that its area can be measured. A glass slide with green dye and cells is used to visualize the shape of the pinhole and focus. (B). Light intensity of the GFP channel with setting used in Msn2 imaging (LED power at 3%), calculated by dividing the measured irradiance by the area of the pinhole. 60 measurements were taken and the one with the highest value (red dot) was used as the intensity (379 mW/cm^2), assuming that at this measurement the sensor was in the optimal position to receive all photons from the light beam. Since our exposure time was 200 ms, the energy per exposure is determined to be 0.076 J/cm^2 .

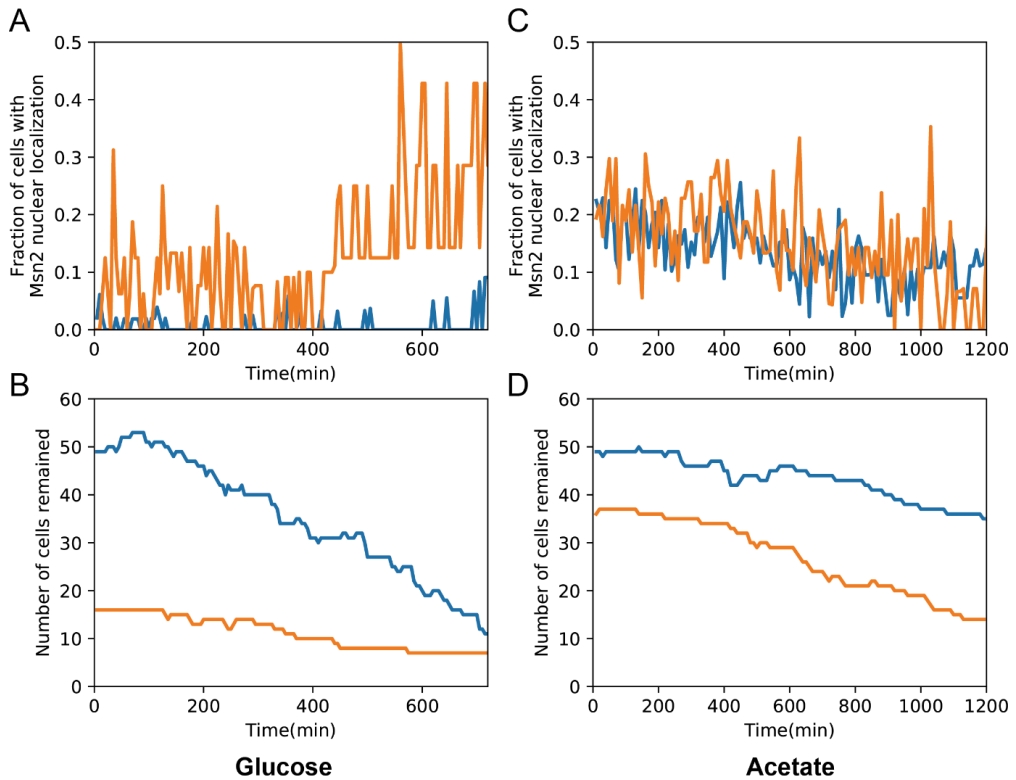


Fig. S3: Msn2 localization over the course of the experiment show no stress induced by microscope light. Corresponding to Fig. 2A, B. (A). The fraction of cells with Msn2 localized in the nucleus throughout the two experiments on glucose condition. Color coding is the same as in Fig. 2A. In one replicate (blue curve), only sporadic Msn2 localization was observed throughout the experiment, indicating no accumulative stress by imaging. In another replicate (orange curve), the fraction seems to increase after ~450 minutes. However, this is likely affected by the small number of cells available in this dataset. (B). Number of cells remained in the analysis and used to calculate the fraction as shown in (A). In the microfluidics, some cells might be flushed away over time when they were, for example, pushed by new born daughter cells. (C). Same as (A), acetate condition. The fraction of Msn2 nuclear localization in both replicates was rather stable throughout the movie and even showed some decrease, indicating no accumulative stress by excitation light. (D). Same as (B), acetate condition.

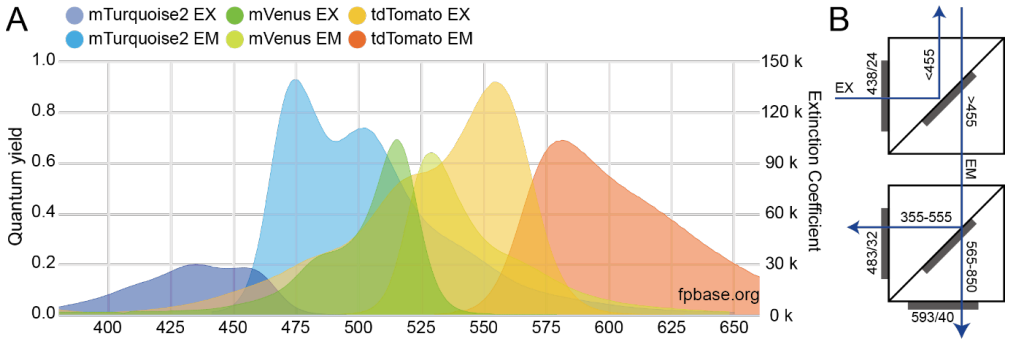


Fig. S4: Spectra of fluorophores and microscope setting. (A). Excitation spectra (indicated as extinction coefficient, right axis) and emission spectra (indicated as quantum yield, left axis) of mTurquoise2, mVenus and tdTomato used in the sensor and mutant strains. Due to the broad spectrum of tdTomato, at the excitation wavelength, the tdTomato still have a significantly high extinction coefficient (e.g., at 438 nm, tdTomato has a value of 8418 while mTurquoise2 has a value of 29478). This figure is generated by the FPbase Spectra Viewer. (B). Filter set used for exciting the yEPAC FRET sensor. For all bandpass filters, spectra are shown as the peak wavelength allowed to pass followed by the light-pass bandwidth. For the dichroic mirrors, spectra are shown as the band range where 95% of light is allowed to pass.

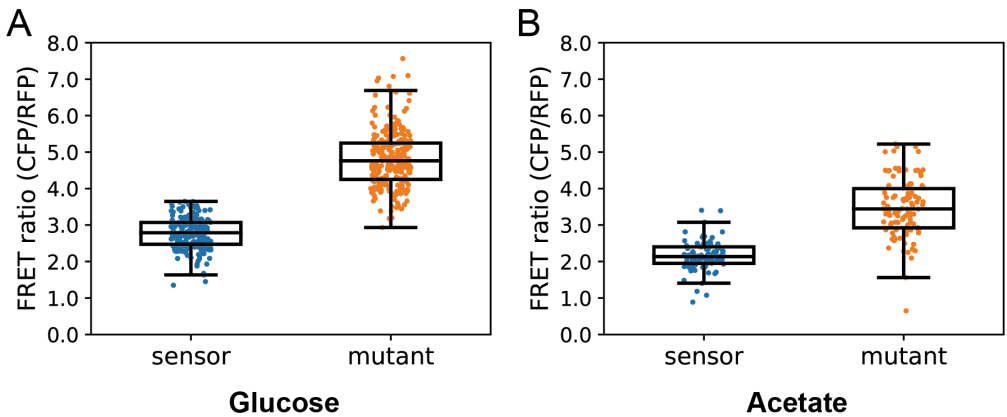


Fig. S5: (uncorrected) FRET ratio of sensor and mutant strains. (A, B). FRET ratio on glucose and acetate conditions, for the sensor and mutant strains. Each dot represents the mean FRET ratio of a cell cycle. On both nutrient conditions, the overall FRET ratio of the mutant strain is higher than the sensor strain. Since the FRET ratio is calculated as the donor to sensor ratio, this suggests less FRET effect in the mutant than the (unbound) sensor.

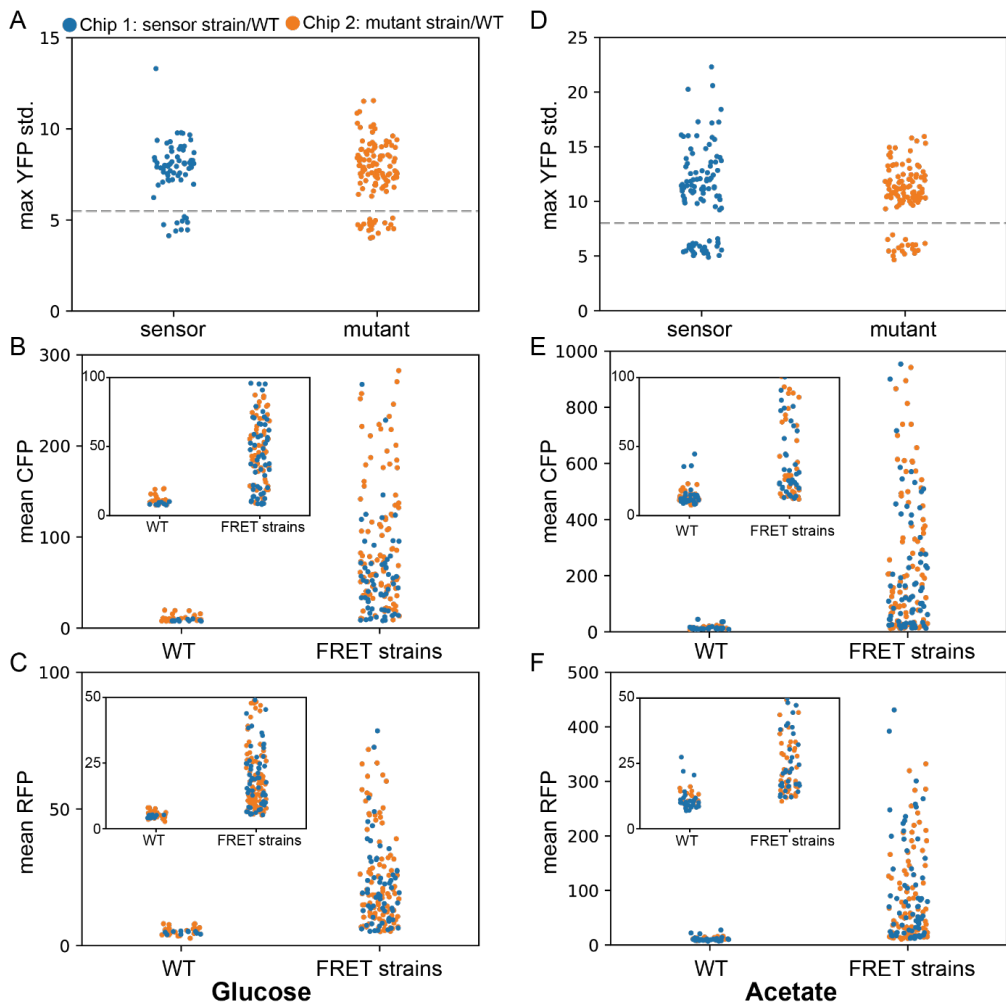


Fig. S6: Differentiating WT cells from FRET cells for determination of autofluorescence. (A-F). Blue dots are cells from chip 1 loaded with sensor strain and WT; orange dots are cells from chip 2 loaded with mutant strain and WT. (A, D). WT cells (without expression of fluorescent proteins) were loaded together with the FRET cells (expressing a YFP tagged *Whi5* cassette besides the FRET sensor/mutant) in the microfluidic chips, and were differentiated using signal of the YFP channel, on acetate or glucose condition. To differentiate the cells, for each segmented cell, standard deviation (over all pixels from the cell) of YFP signal were calculated, and the maximal YFP standard deviation throughout the movie was plotted on the y-axis. For the FRET cells with a YFP tagged *Whi5*, when *Whi5* localized to the nucleus during the cell cycle, the standard deviation will increase. Thus, by drawing a threshold as indicated by the dashed line, the WT and the FRET cells were separated. (B, E). CFP fluorescence intensity of each segmented cell, averaged over all frames throughout the movie, on acetate or glucose condition. WT and FRET cells were differentiated as in (A, D). The inset showed a zoomed-in view of the same plot on y-axis range of 0~100. (C, F). RFP fluorescence intensity of each segmented cell, averaged over all frames throughout the movie, on acetate or glucose condition. WT and FRET cells were differentiated as in (A, D). The inset showed a zoomed-in view of the same plot on y-axis range of 0~50.

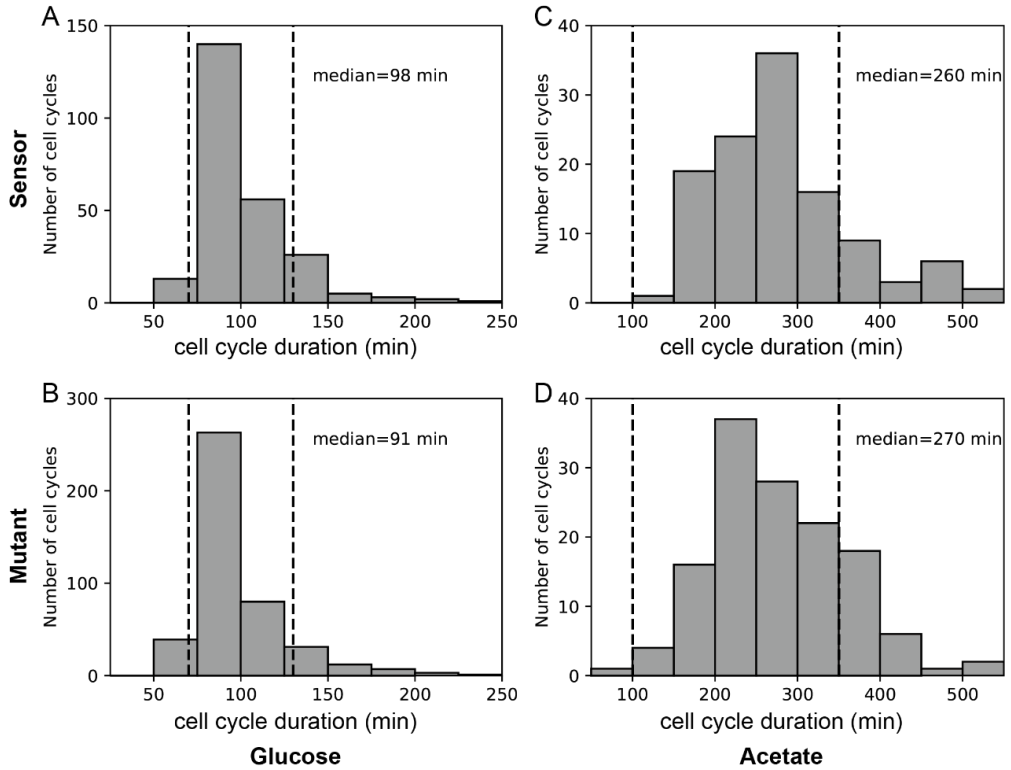


Fig. S7: cell cycle duration and selection. Histogram showing the distribution of cell cycle durations when sensor (A) or mutant (B) cells were grown on glucose, or when sensor (C) or mutant (D) cells were grown on acetate. Median cell cycle duration of each condition is shown. The two dashed vertical lines indicate the range of cell cycle duration of cell cycles that were selected for further analysis, i.e., cell cycles that were either too short or too long were excluded.

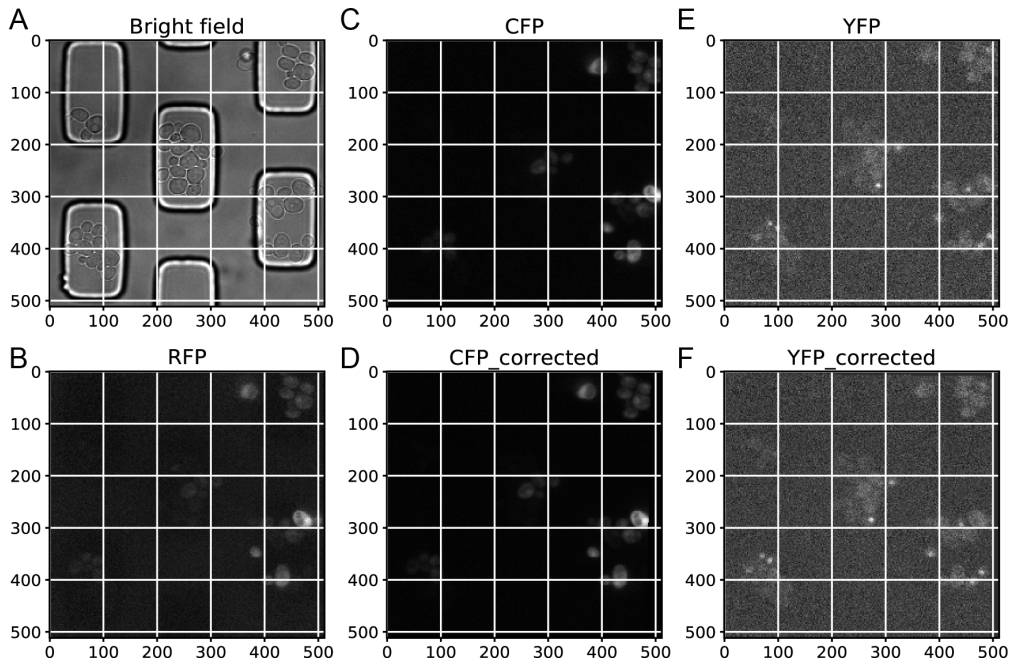


Fig. S8: Channel alignment for FRET imaging. (A). Bright field image of the example field of view used for visualizing the results of channel alignment. The image size is 512 by 512 pixels. Gridlines are shown to aid visual comparisons of cell locations across the different images. (B). RFP image without correction. The RFP channel is captured by the same camera as the bright field channel, and has good alignment with the bright field channel. It is used as the reference image for the CFP and YFP channel. (C). CFP image without correction has misalignment with the bright field and RFP image. (D). After correction, CFP image is aligned with bright field and RFP image. (E). YFP image without correction has misalignment with the bright field and RFP image. (F). After correction, YFP image is aligned with bright field and RFP image.

Supplemental Tables

Table S1: Yeast strains used and/or developed in this study

Strain	Relevant genotype	Related results	Source
YSBN6	FY3 ho::HphMX4	Figure 4	Canelas et al., 2010
YSBN6.G2]	YSBN6: <i>HO::ADH1p-OsTIR1-TEF1p-mGFP-AID-KanMX4</i>	Figure 1, A, D	Papagiannakis et al., 2017
HCY1-1	YSBN6: <i>Msn2-tdGFP</i> <i>Whi5-mCherry</i>	Figure 2, A, C	This study
HCY1-2	YSBN6: <i>Msn2-tdGFP</i> <i>Hta2-mRFP1</i>	Figure 2, B, D	This study
HCY2	YSBN6: <i>Msn2-mVenus</i>	Figure 2, A, C	This study
HCY3	YSBN6: <i>HO::ADH1p-OsTIR1-tADH1-KanMX4</i> <i>Cyr1-mCherry-AID⁷¹⁻¹¹⁴</i> <i>Msn2-mVenus</i>	Figure 1, B, C	This study
HCY4-1	YSBN6: <i>X1::prNOP7-bPAC-CA adh1term</i> <i>HO::ADH1p-OsTIR1-tADH1-KanMX4</i> <i>Cyr1-AID⁷¹⁻¹¹⁴</i> <i>Msn2-mVenus</i>	Figure 1, E, F Figure 5, A, B, C	This study
HCY6-1	YSBN10: <i>Whi5-mVenus</i> pDRF1-GW: <i>URA3,yEPAC</i>	Figure 3, A Figure 4	This study
HCY6-2	YSBN10: <i>Whi5-mVenus</i> pDRF1-GW: <i>URA3,yEPAC-R279L</i>	Figure 3, A Figure 4	This study

Table S2: Primers used for the development, sequencing, and verification of recombinant strains

Primer	Sequence	Functionality
Msn2-rep-27-mVenus-fw	TTTAGTAGAAGCGATAATTTGTCGCAACACATCA AGACTCACAGAAGCATGGACATTATGTTAG TAAAGGTGAAG	Repair primer for tagging Msn2 with mVenus
Msn2-rep-27-mVenus-rv	CATTGAACAGAATTATCTTATGAAGAAAGATCTAT CGAATTAATAAATGGGGTCTATTACTTGATAAT TCATCCATACC	Repair primer for tagging Msn2 with mVenus
Msn2-rep-27-tdGFP-fw	TTTAGTAGAAGCGATAATTTGTCGCAACACATCA AGACTCACAGAAGCATGGACATTGCTGACC GTGCTGTTAATTAAC	Repair primer for tagging Msn2 with tdGFP
Msn2-rep-27-tdGFP-rv	CATTGAACAGAATTATCTTATGAAGAAAGATCTAT CGAATTAATAAATGGGGTCTATTACTTGATAAT TCATCCATACCGTCTG	Repair primer for tagging Msn2 with tdGFP
Msn2-sg-27-fw	GACTTTATCAAGACTCATAAAAAACA	sgRNA for tagging Msn2 using the MoClo CRISPR system
Msn2-sg-27-rv	AAACTGTTTTTATGAGTCTTGATAA	sgRNA for tagging Msn2 using the MoClo CRISPR system
Msn2CDS-fw	TTATGCTCCCGCGCTCGTATGTTGTGTGGCTACA GCCTTGAGTAATGATATGC	Diagnostic primer for confirming Msn2-tagging
Msn2Down-rv	GTTCCAGTTTGAACAAGAGTCCACTATTAAGG GCTTTACCGCTAATAAG	Diagnostic primer for confirming Msn2-tagging
mVenus_co-rv	TTCAATGTTATGTCTAATTTTC	Sequencing of mVenus-tagging
cyr1-IAA-rep-fw	CTGCTCGAAGCAATATTTTCAATGTTGTTGACGAA CTTTTACAAATGGTTAAGAATCCCAAGATTATC AACTGTCGACGGTGCAGGCC	Repair primer for tagging Cyr1 with AID
cyr1-IAA-rep-rv	TTCTCTACGGTGAATATGAAACGAGTAACAGGGT CGTACATAATTTACGAACAGAAGTCAACCGGGT ATACCTTCAC	Repair primer for tagging Cyr1 with AID
cyr1-IAA_YTK_sg-rv	AAACTTGCCTTCTTAACCATTTGTAA	sgRNA for tagging Cyr1 with AID using the MoClo CRISPR system
cyr1-IAA_dg fw	AGAATCGAATCCAGTGTCG	Diagnostic primer for confirming Cyr1-tagging
cyr1-IAA_dg rv	GCCAAATATGAGAGGAGATG	Diagnostic primer for confirming Cyr1-tagging
Cyr1_IAA_seq1	AGAACCTTATCTCTATAGCC	Sequencing of Cyr1-AID construct
bPAC-full-rep-fw	GCAGTTATCTCTGTGCCAGATCCCTTTGAAGTAA AGTTTATCAATTTTCTATAGAACGATGTATCGGG AAACGAAC	Repair primer for integration of bPAC at X1 locus
bPAC-full-rep-rv	CTACAGTAATGTGCGGTGCAGGGAGGCAATGTT TAGTGCATCTCTACATCAATTCTCACCGAGTT GATAACTAAC	Repair primer for integration of bPAC at X1 locus
bPAC-X1_YTK_sg-fw	GACTTTCATACGGCCGAAGCCAATTC	sgRNA for integration of bPAC at X1 locus

bPAC-X1_YTK_sg-rv	AAACGAATTGGCTTCGGCCGTAGCAA	sgRNA for integration of bPAC at X1 locus
X1-dg-fw	ATGTACGGAAAAACGGGTAC	Diagnostic primer for confirming integration of bPAC at X1 locus
X1-dg-rv	TGTCAGCCCATGATATAGC	Diagnostic primer for confirming integration of bPAC at X1 locus
X1_bPAC_seq1	AATCAAATGCGACTTGCC	Sequencing of X1::bPAC construct
bPAC-seq-fw	AGAATAATGTCATGTCGTC	Sequencing of bPAC gene on source plasmid pHES609 (Addgene)
bPAC-seq-rv	TATCGCACTCACGTAAAC	Sequencing of bPAC gene on source plasmid pHES609 (Addgene)
TEFprom rev1	CGAGGAGCCGTAATTTTTGC	Sequencing of various GG3 plasmids
Whi5_sg106-fw	GACTTTCCTCACTTCGGTATCCGACT	sgRNA for tagging Whi5 using the MoClo CRISPR system
Whi5_sg106-rv	AAACAGTCGGATACCGAAGTGGAGAA	sgRNA for tagging Whi5 using the MoClo CRISPR system
Hta2_sg18-fw	GACTTTTTGAGAAGCTTTGGCACTCT	sgRNA for tagging Hta2 using the MoClo CRISPR system
Hta2_sg18-rv	AAACAGACTGCCAAAGCTTCTCAAAA	sgRNA for tagging Hta2 using the MoClo CRISPR system
Whi5-rep106-mVenus-fw_trunc	TGCTGGAGAACCACGGACGAAACGGAGCCCGA AAGCGACACCGAAGTGGAGACGTCTATGTTAGT AAAGGTGAAG	Repairing primer for tagging Whi5 with mVenus
Whi5-rep106-mVenus-rv_trunc	CGGGGCGCGGCTGCACTAACTCCGAGATTGCGG AGAAAAAACTCGTACTACCACATTACTTGTATAAT TCATCCATACC	Repairing primer for tagging Whi5 with mVenus
Hta2-rep18-mRFP1-fw	ATTCACAAAACTTGTGGCCAAAGAAGTCTGCCA AAACAGCAAAAAGCTTCTCAAGAACTGATGGCCT CCTCCGAGGACG	Repairing primer for tagging Hta2 with mRFP1
Hta2-rep18-mRFP1-rv	TTAAAACCCCAATGACAAGAATGTTTGATTTGC TTTGTTCCTTTTCAACTCAGTTCTTAGGCCCCGCT GGAGTGGC	Repairing primer for tagging Hta2 with mRFP1
X1_bPAC_seq1	AATCAAATGCGACTTGCC	Sequencing primer for confirming bPAC X1 integration
Cyr1_IAA_seq1	AGAACCTTATCTCTATAGGC	Sequencing primer for confirming Cyr1 IAA tagging
Whi5-rep106-mCherry-fw	TCTGCTGGAGAACCACGGACGAAACGGAGCCC GAAAGCGACACCGAAGTGGAGACGTCTATCGTG AGCAAGGGCGAG	Repairing primer for tagging Whi5 with mCherry
Whi5-rep106-mCherry-rv	CAGCGGGCGCGGCTGCACTAACTCCGAGATTGCC GAGAAAAAACTCGTACTACCACATTACTTGTACA CCTCGTCCATGC	Repairing primer for tagging Whi5 with mCherry

Table S3: Properties of tested Msn2 localization parameters

Name of localization parameter	Means of determining localization score	Typical values
Elowitz	Difference between the mean intensity of the five brightest pixels in the cell and the mean intensity of all pixels in the cell.	Scores lie around 15-100 (a.u.), with a threshold around 35, where values above this threshold are categorized as nuclear.
Elowitz-median	Difference between the mean intensity of the five brightest pixels in the cell and the median intensity of all pixels in the cell.	Scores lie around 15-100 (a.u.), with a threshold around 35, where values above this threshold are categorized as nuclear.
Stewart	Ratio between the mean intensity of the brightest 10% of pixels in the cell and the median intensity of all pixels in the cell.	Scores lie around 1-5 (a.u.), with a threshold around 1.70, where values above this threshold are categorized as nuclear.
Stewart-mean	Ratio between the mean intensity of the brightest 10% of pixels in the cell and the mean intensity of all pixels in the cell.	Scores lie around 1-5 (a.u.), with a threshold around 1.70, where values above this threshold are categorized as nuclear.
ES-sum	Combines Elowitz (E_{score}) and Stewart (S_{score}) parameter by summing them after scaling the S_{score} by a factor of 21 to bring it into the same order of magnitude as the E_{score} . The sum must pass the ES-sum threshold to be categorized as nuclear localized: $E_{score} + S_{score} * 21 > \text{Threshold}_{ES-sum}$	Scores lie around 40-160 (a.u.), with a threshold around 70, where values above this threshold are categorized as nuclear.
ES-both	Combines Elowitz (E_{score}) and Stewart (S_{score}) parameter by taking their Boolean AND: If ($E_{score} > E_{threshold}$) & ($S_{score} > S_{threshold}$), Msn2 is categorized as nuclear. In all other cases, Msn2 is categorized as cytosolic.	N/A

References

1. Botman, D. *et al.* A yeast FRET biosensor enlightens cAMP signalling. *Mol. Biol. Cell* mbcE20050319 (2021). doi:10.1091/mbc.E20-05-0319
2. de Rooij, J. *et al.* Mechanism of regulation of the Epac family of cAMP-dependent RapGEFs. *J. Biol. Chem.* **275**, 20829–20836 (2000).
3. Ponsioen, B. *et al.* Detecting cAMP-induced Epac activation by fluorescence resonance energy transfer: Epac as a novel cAMP indicator. *EMBO Rep.* **5**, 1176–1180 (2004).

